

MASTER'S THESIS

**Calibration of the Digital Hadron
Calorimeter using Data Track Segment
Analysis**

Isabelle Viarouge

Department of Physics

McGill University, Montreal

2018, April

*A thesis submitted to McGill University in partial fulfillment of the
requirements of the degree of Master's of Science*

©2018 Isabelle Viarouge

*“If you can keep your head when all about you
Are losing theirs and blaming it on you,
If you can trust yourself when all men doubt you,
But make allowance for their doubting too.
If you can wait and not be tired by waiting,
Or being lied about, don’t deal in lies,
Or being hated, don’t give way to hating,
And yet don’t look too good, nor talk too wise:
If you can dream—and not make dreams your master;
If you can think—and not make thoughts your aim;
If you can meet with Triumph and Disaster,
And treat those two impostors just the same;
If you can bear to hear the truth you’ve spoken
Twisted by knaves to make a trap for fools,
Or watch the things you gave your life to, broken,
And stoop and build ’em up with worn-out tools:
If you can make a heap of all your winnings
And risk it on one turn of pitch-and-toss,
And lose, and start again at your beginnings
And never breathe a word about your loss;
If you can force your heart and nerve and sinew
To serve your turn long after they are gone,
And so hold on when there is nothing in you
Except the Will which says to them: “Hold on!”
If you can talk with crowds and keep your virtue,
Or walk with Kings—nor lose the common touch,
If neither foes nor loving friends can hurt you,
If all men count with you, but none too much;
If you can fill the unforgiving minute
With sixty seconds’ worth of distance run,
Yours is the Earth and everything that’s in it,
And—which is more—you’ll be a Man, my son!”*

Rudyard Kipling, *Rewards and Fairies* (1910).

Résumé

Le futur Collisionneur Linéaire International (ILC), un collisionneur électron-positron, a pour mission d'étudier les propriétés du nouveau boson de Higgs découvert au Grand collisionneur de hadrons (LHC) en 2012, en plus d'explorer le domaine des hautes énergies avec une résolution en énergie inégalée. Pour accomplir ce programme ambitieux, la collaboration CALICE développe et recherche de nouveaux designs de calorimètres hadroniques (HCAL) avec une granularité sans précédent pour tirer parti de l'approche algorithmique du suivi de particules (PFA). Le Calorimètre Hadronique Digital (DHCAL) dont un prototype de 1 m^3 a été construit en 2009-2010 au Laboratoire National d'Argonne, USA, fait partie de ces nouveaux calorimètres. Chaque plan de ce HCAL à échantillonnage est fait de trois chambres à plaques résistives (RPCs) dont une des surfaces est recouverte par des cellules de lecture digitale de $1 \times 1 \text{ cm}^2$ qui procurent au DHCAL son excellente résolution spatiale. Le prototype a été exposé à des faisceaux de particules à des énergies allant de 8 GeV à 300 GeV à FermiLab et au CERN en 2011, en utilisant des plaques d'acier et de tungstène comme absorbeurs. Grâce aux capacités d'imagerie du DHCAL, l'identification des segments correspondant aux trajectoires des particules a pu être développée et testée en utilisant les données recueillies à FermiLab en Juin 2011. Un nouveau schéma de calibration utilisant les angles d'entrée des segments a été appliqué aux données avec succès. La stabilité de la réponse du détecteur durant les tests a été vérifiée par les résultats d'une calibration relative de l'ordre de 2.8% suivant le schéma mentionné plus tôt. Bien que la possibilité d'utiliser l'analyse des segments comme schéma de calibration a été démontrée dans cette thèse, il serait intéressant de continuer la validation de ce schéma à l'aide de simulations.

Abstract

The future International Linear Collider (ILC), an electron-positron collider, has for mission to investigate the properties of the new Higgs Boson discovered at the Large Hadronic Collider (LHC) in 2012 in further details, as well as to explore the high energy domain with unmatched energy resolution. To fulfill this ambitious program, the CALICE collaboration is developing and researching new hadronic calorimeter (HCAL) designs with unprecedented granularity to make the most of the Particle Flow Algorithm (PFA) approach. One such HCAL is the Digital Hadronic Calorimeter (DHCAL) of which a 1 m^3 prototype was built in 2009-2010 at Argonne National Laboratory. Each layer of this sampling HCAL is made of three Resistive Plate Chambers (RPCs) whose surface is spanned by $1 \times 1 \text{ cm}^2$ digital read-out cells granting excellent spatial resolution to the DHCAL. The prototype was exposed to test beams at energies ranging from 8 GeV to 300 GeV at FermiLab and CERN in 2011 using steel and tungsten absorber layers. Making use of the imaging capabilities of the DHCAL, track segment identification was developed and tested using the FermiLab data from June 2011. A new calibration scheme using track segment analysis was applied to the data with success. The stable response of the DHCAL during the test beams was established at an order of 2.8% level using the findings of a relative calibration following the mentioned scheme. While the possibility of using track segment analysis as a calibration scheme were explored here, further validation with the help of simulation is suggested.

Acknowledgements

I would like to express my gratitude to my supervisor François Corriveau for his guidance, his patience, his encouragements and the wonderful discussions we shared in his office.

Many thanks go to Paul Mercure who was always ready to help me with any computer issue I was able to conjure on my desk computer.

I would like to thank the wonderful people I met during my research and with whom I shared my office. They made my master years fun and enjoyable, and they increased my social life by 10 points at least.

I want to thank my amazing roommates Simone and Cristina who listened patiently to my rants when I was having difficulty with my research and always encouraged me to continue.

It is very hard to put into words the gratitude I want to express to my closest friends Andrea, Amine, Dounia, Léopold and Pierrick. Each, in their way, have contributed to this thesis whether by hosting video game and pizza nights, or accompanying me on crazy escapades to ride mechanical bulls, or simply being there to listen to my philosophical conundrums.

Lastly, I would like to express my gratitude to my parents and thank them for everything. Without them, I most certainly would not be writing these lines, thus turning the page on yet another chapter in my life.

Contents

Résumé	ii
Abstract	iii
Acknowledgements	iv
1 Introduction	1
2 The Standard Model	3
2.1 A Brief History of Particle Physics	3
2.1.1 Early Ideas	3
2.1.2 Atoms and Nucleons	3
2.1.3 1930s to 1970s: Discovery of a Zoo of Particles	4
2.1.4 Modern Particle Physics and the Standard Model	4
2.2 The Standard Model	4
2.3 Shortcomings of the Standard Model	5
3 The International Linear Collider	7
3.1 ILC Design	8
3.1.1 Two Detectors Based on Particle Flow Analysis	9
PFA: A General Philosophy	9
SiD (Silicon Detector)	10
ILD (International Large Detector)	10
4 Particle Interaction in Matter	13
4.1 Interaction of Particles With Matter	13
4.1.1 Ionization	13
4.1.2 Bremsstrahlung Radiation	15
4.1.3 Compton Scattering	16
4.1.4 Pair Production	17

4.2	Particles	17
4.2.1	Electrons and Positrons	18
4.2.2	Muons	18
4.2.3	Photons	19
4.2.4	Hadrons	19
4.3	Showers	20
4.3.1	Electromagnetic Shower	20
4.3.2	Hadronic Shower	22
4.4	Energy Resolution	23
5	Calorimetry and CALICE Detectors	25
5.1	Calorimetry	25
5.1.1	Homogeneous Calorimeter	26
5.1.2	Sampling Calorimeter	26
5.2	AHCAL	27
5.2.1	Overview of the Prototype	27
5.2.2	Strengths and Weaknesses	27
5.3	SDHCAL	28
5.3.1	Overview of the Prototype	28
5.3.2	Strengths and Weaknesses	28
5.4	DHCAL	29
5.4.1	Overview of the Prototype	29
5.4.2	Technical details and Fermilab Configuration	30
5.4.3	Energies and Data Format	31
5.4.4	Strengths and Weaknesses	33
6	Event Selection	34
6.1	Faulty Events and the Associated Cuts	34
6.1.1	Too Few Hits and Too Many Hits	35
6.1.2	Faulty Layer	35
6.1.3	Early Showering	35
6.1.4	Multiple Entries	35
6.2	Surviving Events and Particle Identification	40
6.2.1	Identification Parameters	40
6.2.2	Muons	42
6.2.3	Pions	42

6.2.4	Electrons/Positrons	42
6.2.5	Surviving Events	46
7	Calibration	48
7.1	Efficiency	48
7.2	Multiplicity	49
7.3	Calibration factor	49
7.4	Overall calibration factor	49
8	Track Segment Analysis	50
8.1	Track Segments Analysis in CALICE Calorimeters	50
8.1.1	AHCAL	50
8.1.2	SDHCAL	50
8.1.3	DHCAL	51
8.2	Segment Selection	51
8.2.1	Identifying Clusters	51
8.2.2	Segment Selection	52
8.2.3	Tuning of NHits	53
8.3	Combining Segments and Single Hits	60
8.3.1	Tuning of RADI	60
8.4	Calibration Scheme: Track Segment Angles	64
8.4.1	Motivation	64
8.4.2	Calibration Factors	65
8.4.3	Relative Calibration Results	67
9	Discussion and Conclusion	81
	Bibliography	83
	List of Abbreviations	86

To my parents.

Chapter 1

Introduction

Particle physics investigates the building blocks of matter, the particles and their interactions in hope of achieving a better understanding of the world we live in. To pursue this goal, particle accelerators collide particles at higher and higher energies in search of new fundamental particles and their corresponding interactions with known matter. In 2012, the Higgs Boson postulated in the 60s was found at the Large Hadron Collider (LHC), prompting the need to investigate its properties with better precision than a proton-proton collider can offer.

The future International Linear Collider (ILC), presently awaiting construction, will be a new electron-positron collider with the necessary precision and nominal beam energy to not only investigate the properties of the discovered Higgs boson but also look for new physics at the TeV energy scale. The innovative calorimeter design based on high granularity will grant the excellent energy resolution ambitioned by the ILC. Three such designs based on different technologies were developed and researched by the CALICE collaboration for the ILC hadron calorimeters: the Analog Hadron Calorimeter (AHCAL), the Semi-Digital Hadron Calorimeter (SHDCAL) and the Digital Hadronic Calorimeter (DHCAL).

This thesis presents the analysis of the test beam data of the DHCAL prototype built at Argonne National Laboratory in 2009-2010 with data taken in June 2011 at FermiLab. A new track segment calibration scheme based on the efforts of the CALICE collaboration to achieve in-situ track segment calibration in their new calorimeters, was selected and tested. Previous work at McGill University was undergone on the calibration of DHCAL using dedicated muon runs with the minimal configuration (minDHCAL)[16]

at lower energies, and a preliminary study of track segment identification and calibration[15] was also completed. The work presented in this thesis expands on the identification of the track segments and their selection, as well as display their power to monitor the detector response in-situ in the context of non-zero polar angle track segment calibration.

Chapter 2

The Standard Model

2.1 A Brief History of Particle Physics

2.1.1 Early Ideas

The idea that matter is made of fundamental building blocks appears as early as the 5th century BC with the philosophical doctrine of Atomism. Coming from the Greek word for indivisible, *ἄτομος*, atoms are thought to come in many shapes and sizes by the scholar atomists. However, this theory is not based on experimental evidence but pure intuition. Experimental confirmation has to wait the 19th century when the stoichiometric experiments of the chemist John Dalton suggested that elements are made of fundamental particles which he named atoms [6].

2.1.2 Atoms and Nucleons

Science soon rectifies Dalton's insight as his atoms are really molecules made of smaller particles, the atoms whose structure intrigues scientists. In 1897, J. J. Thomson notices that the application of a magnetic field next to a cathodic ray bends the latter. Following more experimentation, he discovers the electrons, small negatively charged particles which he theorizes to be part of the atomic nucleus in a similar way as plums in a positively charged pudding. The Plum Pudding model is replaced by the solar system model after the Rutherford gold foil experiment in 1907 illustrated that atoms are mainly made of empty space save for a very tiny and positively charged nucleus[17].

2.1.3 1930s to 1970s: Discovery of a Zoo of Particles

The beginning of the 20th century corresponds to a golden age of particle physics as the understanding of quantum mechanics and the improvement of particle accelerators let physicists explore energies up to the MeV scale. The formulation of quantum field theory (QFT) introduces the concept of fermions, bosons and fundamental bosons acting as force carriers. For example, the photon is promoted to electromagnetic force carrier in quantum electrodynamics (QED). Soon, many particles are discovered between 1930 and 1950 such as the muon lepton, the charged pion meson, the neutral pion and strange particles. The surprisingly high number of new fundamental particles suggests that most of these new particles are actually composites of even more fundamental particles: the quarks and the gluons. This is the birth of quantum chromodynamics (QCD) [17].

2.1.4 Modern Particle Physics and the Standard Model

Throughout the 20th century, particle physicists try to formulate a "theory of everything" which would unify all theories that describe the physical world, all its particles and its fundamental interactions: the electromagnetic force, the weak force, the strong force and the gravitational force. In the 1970s, Abdus Salam, Steven Weinberg and Sheldon Glashow successfully unite the weak and electromagnetic force into the electroweak theory. Shortly after, a united field theory including all fundamental interaction but gravitation is formulated: the Standard Model [17].

2.2 The Standard Model

The Standard Model is an effective field theory which describes three out of four of the fundamental forces, namely: the electromagnetic force and the weak force now united into the electroweak force, and the strong force while leaving out the gravitational force. These fundamental forces are the consequence of the interactions of force carrier particles, the gauge bosons, with the various particles constituting matter. The photon mediates the electromagnetic force, the W^\pm and Z^0 bosons the weak force and the gluon is the messenger particle of the strong force. Fundamental particles are classified

into two families, the fermions and the bosons. A boson is a particle with integer spin while a fermion has half integer spin. Elementary fermions can be further classified into three generations of matter comprised of quarks, leptons and their corresponding antiparticles as illustrated by the table of elementary particles in Figure 2.1. The success of the Standard Model lies in its power to predict the outcome of particle interactions with great accuracy. The Higgs boson predicted by the Standard Model should be mentioned as the theory's most recent success. In order to give masses to gauge bosons, the Higgs particle was added to the Standard Model in the 60s to later be discovered in 2012 at the Large Hadron Collider (LHC) at CERN, the largest particle accelerator in the world [4, 17, 21].

2.3 Shortcomings of the Standard Model

While the Standard Model has been established as the best description of the fundamental interactions at the subatomic scale during these past decades, there are still experimental observations that do not find their explanations. First and foremost is the lack of gravity in the Standard Model, the most readily visible force at human scale. Then, the phenomenon of neutrino oscillations contradicts the Standard Model. These oscillations between neutrino flavors are only possible if neutrinos have mass which they are not predicted to have in the Standard Model. Another illustration is the lack of candidates for dark matter, a theorized type of matter that does not interact electromagnetically but is responsible for gravitational lensing among other gravitational phenomena unexplained without its introduction. This unique type of matter accounts for 26.8% of the universe mass-energy while the matter described in the Standard Model only accounts for 4.9%. In light of these problematic aspects of the Standard Model, the need to build new accelerators that can investigate higher energy scales is still of actuality. Not only will building more powerful colliders bring insights into these unanswered questions, but it will also help better understand the physics discovered thus far and potentially uncover new particles [4, 17, 21].

Standard Model of Elementary Particles

		three generations of matter (fermions)				
		I	II	III		
mass		$\approx 2.4 \text{ MeV}/c^2$	$\approx 1.275 \text{ GeV}/c^2$	$\approx 172.44 \text{ GeV}/c^2$	0	$\approx 125.09 \text{ GeV}/c^2$
charge		$2/3$	$2/3$	$2/3$	0	0
spin		$1/2$	$1/2$	$1/2$	1	0
		u up	c charm	t top	g gluon	H Higgs
	QUARKS	$\approx 4.8 \text{ MeV}/c^2$	$\approx 95 \text{ MeV}/c^2$	$\approx 4.18 \text{ GeV}/c^2$	0	
		$-1/3$	$-1/3$	$-1/3$	0	
		$1/2$	$1/2$	$1/2$	1	
		d down	s strange	b bottom	γ photon	
		$\approx 0.511 \text{ MeV}/c^2$	$\approx 105.67 \text{ MeV}/c^2$	$\approx 1.7768 \text{ GeV}/c^2$	$\approx 91.19 \text{ GeV}/c^2$	
		-1	-1	-1	0	
		$1/2$	$1/2$	$1/2$	1	
		e electron	μ muon	τ tau	Z Z boson	
	LEPTONS	$< 2.2 \text{ eV}/c^2$	$< 1.7 \text{ MeV}/c^2$	$< 15.5 \text{ MeV}/c^2$	$\approx 80.39 \text{ GeV}/c^2$	
		0	0	0	± 1	
		$1/2$	$1/2$	$1/2$	1	
		ν_e electron neutrino	ν_μ muon neutrino	ν_τ tau neutrino	W W boson	
						SCALAR BOSONS
						GAUGE BOSONS

FIGURE 2.1: Classification table of the elementary particles. The fermions and bosons are divided into three generations of quarks, leptons and their antiparticles. The remaining elementary particles are the force messengers, the gauge bosons where the Higgs holds a special place as the only fundamental scalar boson [23].

Chapter 3

The International Linear Collider

After the discovery of the Higgs boson at the LHC in 2012, the need to study its properties and processes with better precision and to address physics beyond the Standard Model has motivated the study of future electron-positron linear accelerator designs. Such designs would avoid the energy loss of the particles through synchrotron radiation. While the operating energies of such accelerators would be lower than at the LHC, the beam energy would be entirely converted into collision energy which is generally not true for proton-proton colliders. Indeed, protons are composite particles made of quarks and gluons. During a proton-proton collision, the beam energy is spread among the quarks which have an associated probability to collide with the quarks of the other incoming proton. In effect, only the fraction of beam energy carried by the interacting quarks is used. While it is in principle possible to observe an interaction at beam energy it has a very low probability. Thus, the interactions observed by the LHC are mostly at an energy lower than beam energy. This is adverted in a electron-positron collision where beam energy goes entirely into the interaction of these elementary particles, avoiding the background and color flow associated to quark/quark collisions of two hadrons colliding. To this date, two projects of electron-positron linear colliders distinguish themselves from the others: the International Linear Collider (ILC) and the Compact Linear Collider (CLIC) at CERN under the supervision of the Linear Collider Collaboration (LCC) [4].

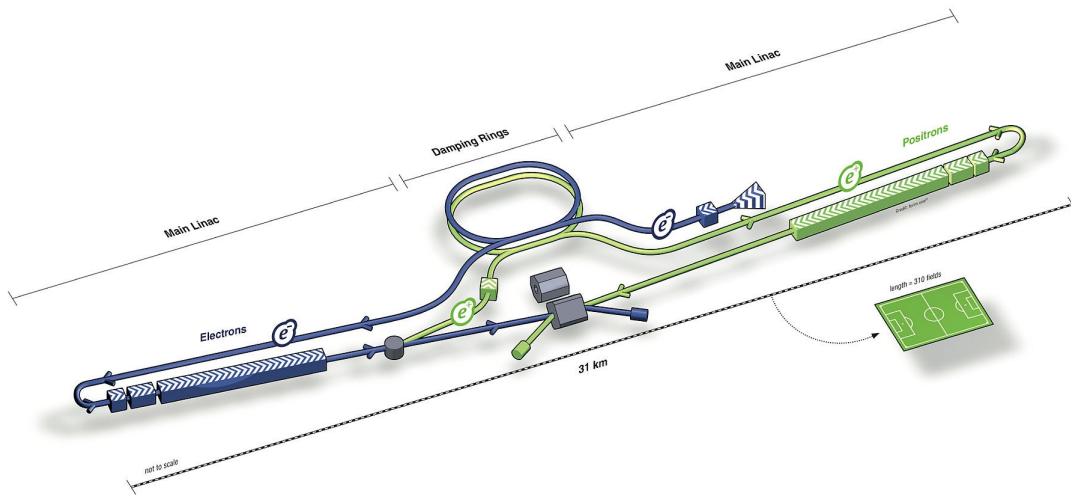


FIGURE 3.1: ILC baseline design. Electrons and positrons are injected into two damping rings before undergoing accelerations in the two linacs until they reach a collision site where a detector will measure the products [3].

3.1 ILC Design

Technical reports have been issued presenting a general design for the electron-positron collider which is summarized in Figure 3.1. At present, the ILC is still awaiting the political decision to start the construction phase. The construction should take 9 years and the operation period is estimated to be 20 years. The whole accelerator, which will be located in the Iwate prefecture, Japan, is 31 km long and includes [3, 29]:

- A polarized electron source
which delivers a train of 1312 bunches of 2.0×10^{10} electrons each at 5 Hz with a polarization greater than 80%. The illumination of a photocathode in a DC gun by a laser creates the required beam of electrons whose polarization is then rotated by the magnetic fields generated by superconducting solenoids.
- An undulator-based positron source.
The electron beam exiting the main linac goes through a 147 m helical undulator and produces high energy photons (10 to 30 MeV). These photons are then guided to a Ti-alloy target where positrons and electrons are produced in the resulting electromagnetic shower. The positrons are separated from the shower products and accelerated toward the damping rings.

- Beam transport and a two-stage compressor whose responsibility is to keep the low emittance of the beam and produce bunch trains of 1312 bunches per train of length approximately 500 ns at 5 Hz on entry to the main linacs.
- Two Damping rings at 5 GeV and with a circumference of 3.2 km store the electrons (positrons) and achieve a high luminosity and ultra low emittance beam before injection into the beam transport towards the main linacs.
- Two main linacs each 11 km long which will be able to accelerate the positrons and electrons to 500 GeV up to 1 TeV. The technology used for the acceleration of the particles is based on superconducting radio frequency niobium cavities running at 1.3 GHz, operating at a pulse of 1.6 ms in duration.
- Two detectors mounted on a push-pull system, allowing one detector into the beam line to collect experimental data while the other is in a specifically designed hall, accessible for maintenance.

3.1.1 Two Detectors Based on Particle Flow Analysis

In order to fulfill its purpose of probing physics beyond the Standard Model and research the properties of the Higgs boson discovered at the LHC, the ILC must be equipped with cutting edge detectors capable of high energy resolution and visualization power. In recent years, the Particle Flow Algorithm (PFA) has been able to bring a solution to these two requirements.

PFA: A General Philosophy

Traditionally, the energy resolution is limited by the hadronic calorimeter (HCAL) which measures on average 72% of an event energy as studies on the Large Electron-Positron Collider (LEP) showed [26]. The PFA approach proposes to reconstruct event energy by summing the four-vectors of all the particles identified by their tracks in the detector. To reduce the impact of the HCAL low energy resolution, it specializes

in measuring the neutral hadrons in collaboration with the electromagnetic calorimeter (ECAL) while the momenta of charged particles is measured by the trackers and the photons are measured mostly by the ECAL[3]. This scheme relies heavily on accurate particle identification which becomes possible in high granular calorimeters where track imagery is excellent. Indeed, the main limitations of any PFA approach comes from confusion with respect to matching the right track to the right type of particle, and threshold considerations when detecting particles in a high magnetic field in presence of signal background[27]. While PFA is already used at some level in modern detectors such as ATLAS and CMS at the LHC, the ILC detectors will be built around the PFA approach from the start.

SiD (Silicon Detector)

The Silicon Detector (SiD) is a compact all-purpose hermetic detector designed with PFA in mind. Its barrel would have an outer radius of 6.042 m. Dedicated reconstruction of charged particle tracks and neutral particle tracks from the production of secondary charged particles, will be made possible by its finely segmented HCAL and ECAL. As its name implies, this detector makes the most of silicon's high resolution for charged particle tracking. The Vertex detector, ECAL and trackers are made of silicon pixels, allowing for the recreation of a good particle track through imaging techniques. The ECAL would have an inner radius of 1.27 m and a length of 1.76 m. Meanwhile, the HCAL uses Resistive Plate Chambers (RPC) technology to record charged and neutral particle tracks. To allow for a PFA approach, the HCAL has its $10^2 m^3$ total cylindrical volume segmented into 4×10^7 readout pads of size $1 \times 1 cm^2$. Such an HCAL is similar to the Digital Hadron Calorimeter or DHCAL, described later in this thesis. Both calorimeters and the trackers are encased in the 5T magnetic field generating solenoid while the muon trackers form the outer layer of the detector. In order to fulfill the specifications in term of precision, especially in the Higgs sector, the momentum resolution should be at the level of $(1/p_T) \sim 2 - 5 \times 10^{-5}/GeV$ [1].

ILD (International Large Detector)

The second experiment located at the ILC is the International Large Detector (ILD), an all-purpose 4π detector whose design is also based with PFA in mind to achieve

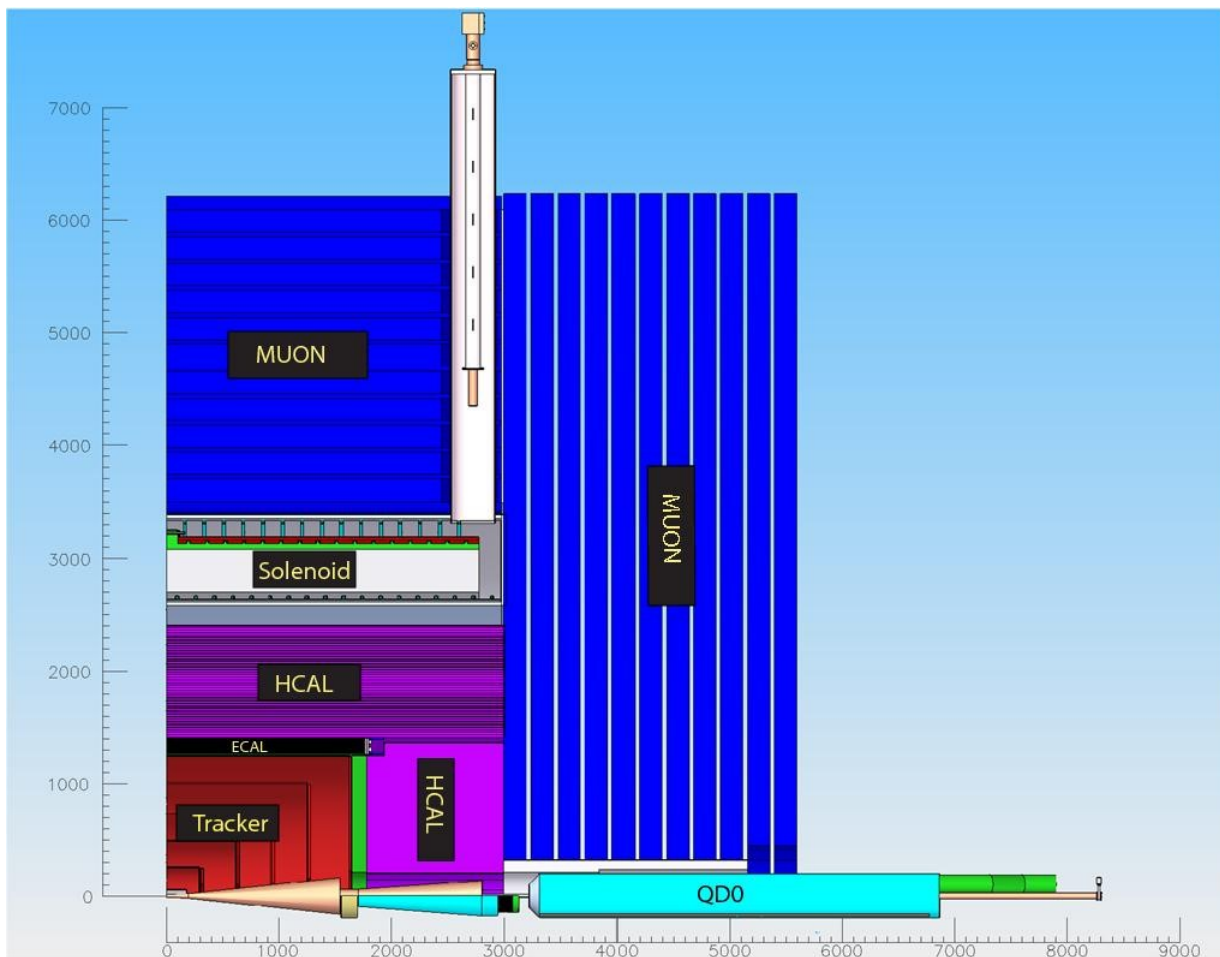


FIGURE 3.2: Profile view of the many components of the SiD [1].

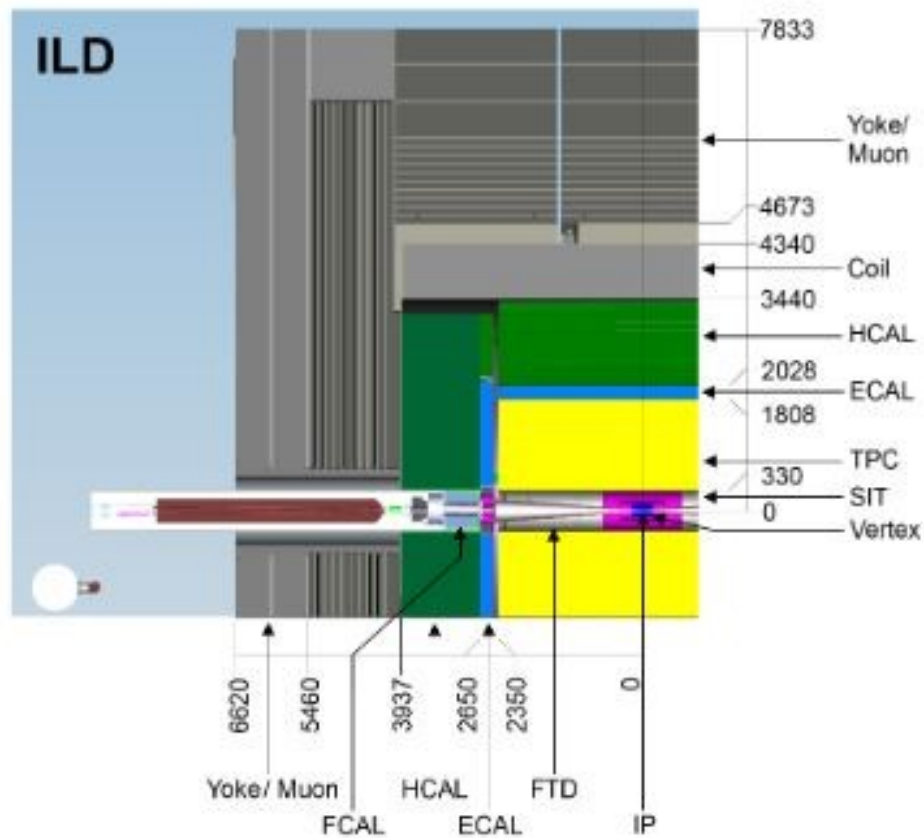


FIGURE 3.3: Profile view of the many components of the ILD [1].

high energy resolution. In its central region, the silicon time projection chamber acts as a tracker while the finely segmented calorimeters (ECAL and HCAL) allows for a first particle identification with excellent jet-energy resolution. The ECAL would be a combination of silicon pad diodes and scintillating strips with silicon photosensor readout and have an outer radius of 2.028 m. While the HCAL with an outer radius of 3.410 m will most definitely use iron as absorber medium, two technologies are still discussed to perform the tracking and energy measurements: scintillator tiles with silicon photosensors and analogue readout electronics or RPCs with two-bit (semi-digital) readout with finer granularity. The outer layer is formed by the 3.5 T magnetic field producing solenoid and the muon iron return yoke which also acts as a tail catcher for the calorimeters and has an outer radius of 7.755 m and a length of 28 m. In order to separate the hadronic decays of the W and the Z , the jet energy resolution needs to be of $\frac{30\%}{\sqrt{E(\text{GeV})}}$ at 100 GeV [1].

Chapter 4

Particle Interaction in Matter

The study of new physics via colliding particles at high energies in larger and more energetic colliders depends on the ability to detect the newly created particles with better accuracy and precision. Calorimetry offers a way to detect a particle by measuring the energy deposited by its passage through an assortment of active and absorbing layers and reconstruct events by assigning the energies to the corresponding type of particle.

4.1 Interaction of Particles With Matter

Particles come in many charges and masses while also being observed at all energy ranges. Therefore, it is expected that their interactions with matter share a similarly rich diversity, a diversity which is reflected in the designs of the particle detectors. In the specific case of calorimetry, the characteristics of the particle interactions with matter dictate the calorimeters' depth, width and choice of material. Only the main interactions through which particles or certain types of particles of interest lose most of their energy will be discussed.

4.1.1 Ionization

An atom or molecule undergoing ionization gains a negative charge or a positive charge because it received or lost one or more electrons. This process can be the product of the collisions between charged incoming energetic particles and the atoms of the detector active medium. It is the main energy loss mechanism for heavy charged particles (many times heavier than an electron) such as muons and pions. In this case,

the energy loss is tightly correlated to the atomic properties of the medium and the incoming particles type and path length in said medium. The Bethe-Bloch formula gives a good estimate of the average energy loss dE per path length dx [19]:

$$-\frac{dE}{dx} = \frac{4\pi N_A r_e^2 m_e c^2 z^2 Z}{A} \left(\frac{1}{\beta^2} \right) \left(\ln \left(\frac{2m_e c^2 \gamma^2 \beta^2}{I} \right) - \beta^2 - \frac{\delta}{2} \right) \left[\frac{\text{MeV}}{\text{g/cm}^2} \right] \quad (4.1)$$

Where :

N_A : Avogadro's number

r_e : classical electron radius

m_e : electron mass

z : incident particle charge

Z, A : atomic number and atomic weight of the absorber material

I : mean excitation energy of the absorber material

β : velocity of the incoming particle $\beta = \frac{v}{c}$

γ : Lorentz factor $\gamma = \frac{1}{\sqrt{1-\beta^2}}$

δ : density correction factor depending on the absorber material

This formula is accurate to a few % for incoming particle energies in the MeV range up to the hundreds of GeV. In this energy range, the average energy loss decreases as $1/\beta^2$ as the incoming particle energy increases until hitting a minimum as illustrated by the stopping power curve for a muon in copper in Figure 4.1. A particle experiencing this minimal energy loss via ionization is described as a *Minimum Ionizing Particle* or MIP. Past this point, the average energy loss increases as the incoming particle energy increases, this is the relativistic rise. Soon, radiative processes dominates such as Bremsstrahlung for charged particles. Note that the ionization processes undergone by electrons and positrons is slightly different than for heavier charged particles. Electrons' and positrons' small mass makes them more susceptible to scatter with large angles and to experience significant energy loss via collisions. As a result, they have a smaller relativistic rise and lose more energy when undergoing bremsstrahlung. To account for these effects and the indistinguishability of electrons and positrons, the Bethe-Bloch formula must be corrected when used for these particles:

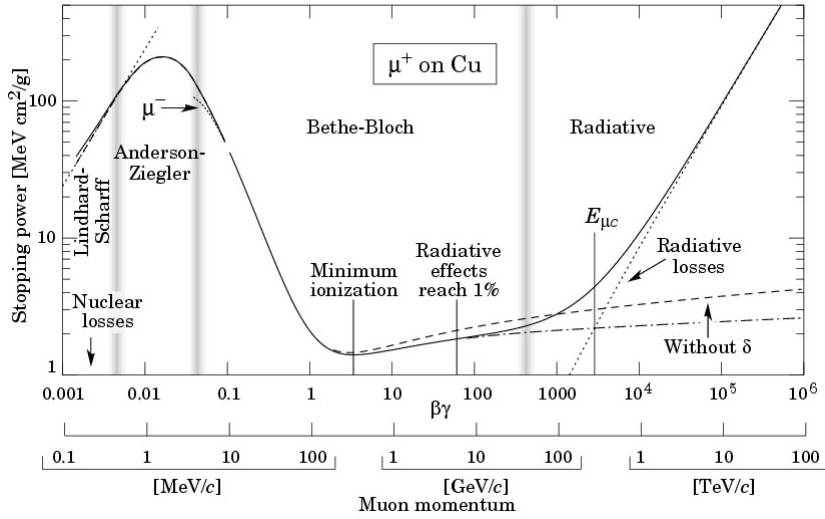


FIGURE 4.1: Stopping power of a muon in copper as a function of muon momentum where $p = M_\mu \beta \gamma c$ where M_μ is the muon's rest mass[18].

$$-\frac{dE}{dx} = \frac{4\pi N_A r_e^2 m_e c^2 z^2 Z}{A\beta^2} \left[\ln \frac{\gamma m_e c^2 \beta \sqrt{\gamma-1}}{\sqrt{2}I} + \frac{1-\beta^2}{2} - \frac{2\gamma-1}{2\gamma^2} \ln 2 + \frac{1}{16} \frac{\gamma-1^2}{\gamma} \right] \left[\frac{\text{MeV}}{\text{g/cm}^2} \right] \quad (4.2)$$

4.1.2 Bremsstrahlung Radiation

Fast charged particles can also interact with the nuclei of the detector's matter via their Coulomb field. The latter decelerates the fast traveling particles, effectively decreasing their energy as the incoming particles emit photons corresponding to that missing energy. At high energies, the average energy loss is approximated as [19]:

$$-\frac{dE}{dx} \approx 4\alpha \left(\frac{1}{4\pi\epsilon_0} \frac{e^2}{Mc^2} \right)^2 \left(\frac{N_A Z^2}{A} \right) z^2 E \ln \left(\frac{183}{Z^{1/3}} \right) \quad (4.3)$$

Where:

α : fine structure constant

ϵ_0 : permittivity of free space

e : elementary charge

M, E : mass and energy of the incoming particle

Others as in equation 4.1.

It can be noted that the average energy loss due to Bremsstrahlung grows as an inverse quadratic of the incoming particle mass, suggesting that lighter particles are more susceptible to lose energy via this mechanism at the high energies expected in a collider. Indeed, Bremsstrahlung is the main energy dissipation mechanism of electrons and positrons at high energies. If collision loss is neglected and only Bremsstrahlung is considered, the mean energy E of a highly energetic electron can be approximated as a decreasing exponential function of its initial energy E_0 and its radiation length which depends on the atomic properties of the absorber medium [19]:

$$E = E_0 e^{-\frac{x}{X_0}} \quad (4.4)$$

Where:

x : path length in the absorber medium

X_0 : Radiation length for this specific medium

With

$$X_0 = \frac{716.4A}{Z(Z+1) \ln(287/\sqrt{Z})} \left[\frac{g}{cm^2} \right] \quad (4.5)$$

The radiation length can be thought as the mean distance traveled by high energy electron for it to radiate all but $\frac{1}{e}$ of its energy by Bremsstrahlung. It is a convenient quantity which enables energy loss to be expressed independently of material characteristics; one only needs to look up a table to find the X_0 of the material needed and to precise the path length or thickness of material traversed. The interaction length appearing later in equation 4.10 is a similar quantity in this respect.

4.1.3 Compton Scattering

Compton scattering is the result of the inelastic collision of a photon with a free or quasi-free charged particle. A fraction of the incident photon energy E is transferred to the charged particle resulting in an increase of the scattered photon wavelength. The

latter also has a lower energy E' :

$$\frac{E'}{E} = \frac{1}{1 + \frac{E}{m_p c^2} (1 - \cos \theta)} \quad (4.6)$$

Where:

m_p : mass of the charged particle

θ : scattering angle of the photon

4.1.4 Pair Production

Pair production is the phenomenon by which a pair of antiparticles are created from a neutrally charged boson. Generally, this term is applied to the production of an electron-positron pair via the interaction between a high energy photon and a nucleus. For pair production to occur, the boson energy must be larger than the total rest mass energies of the antiparticle pair. In the photon/electron-positron case, the threshold energy E_T [19]:

$$E_T = 2m_e c^2 \left(1 + \frac{m_e c^2}{m_r c^2} \right) \quad (4.7)$$

Where:

m_r : rest mass of the nucleus

4.2 Particles

The particles discussed in this section are restricted to the main ones observed in an $e^- e^+$ collider, namely the electrons and positrons constituting the beam and the products of their interactions in the calorimeter. Muons, photons and hadrons are all expected to be part of these secondary particles that need to be slowed down in the detector to estimate accurately their energies.

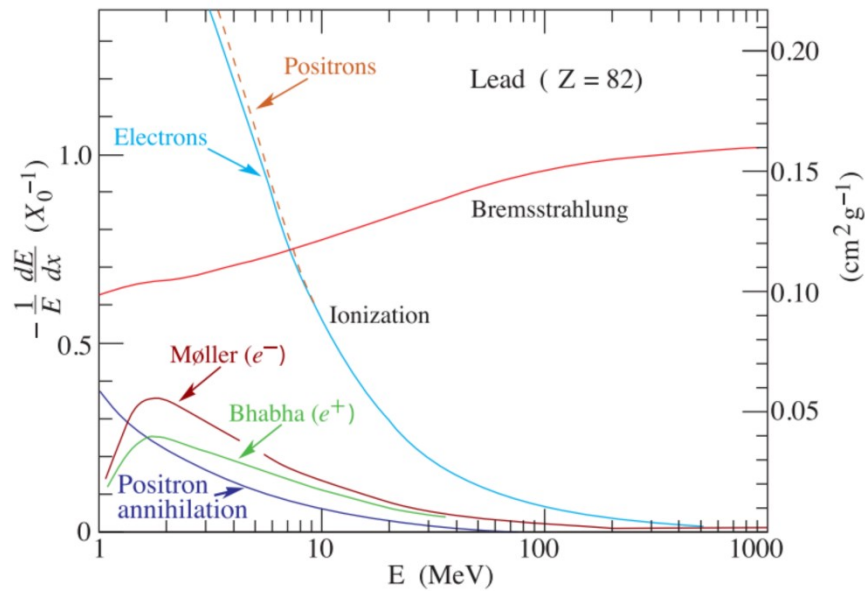


FIGURE 4.2: Stopping power of electrons and positrons as a function of energy in lead [18].

4.2.1 Electrons and Positrons

Figure 4.2 summarizes the main dissipative processes undergone by positrons and electrons through matter in the specific case where these particles are traveling through lead. Ionization dominates at lower energies, as it can be seen in Figure 4.2, well above Møller scattering (electron-electron) and Bhabha (electron-positron) scattering. Past the critical energy mentioned in Section 4.1, Bremsstrahlung becomes preponderant which can lead to electromagnetic showers when the secondary photons are energetic enough to undergo pair production.

4.2.2 Muons

Muon energy loss follows the Bethe-Bloch equation from Section 4.1 and Figure 4.1 illustrates the dissipative processes of muons traveling through copper. After the ionization region at low energies, the energy lost by muons through matter quickly reaches a minimum where they are considered MIPs. In this case, muons go straight through the detectors, interacting weakly within detector medium. At higher energies in the TeV scale, Bremsstrahlung becomes the main dissipative process. In general, muons

act as MIPs in calorimeters and are rarely energetic enough to be observed undergoing Bremsstrahlung (in the TeV scale). In addition, no neutrino-less muon decays are allowed in the Standard Model which forbids the formation of electromagnetic or hadronic showers discussed in section 4.3 [5].

4.2.3 Photons

Photons are either scattered via Compton scattering or absorbed completely by the traversed matter. Consequently, photon detection is done indirectly by detecting the products of photon interactions. The concept of range is undefined in this case but it is possible to approximate the behaviour of photons as the attenuation of a photon beam of initial intensity I_0 through a depth x of absorber material [19]:

$$I(x) = I_0 e^{-\frac{x}{x_p}} \quad (4.8)$$

Where:

x_p : photon path length in the absorber medium

With:

$$x_p = \frac{9}{7} X_0 \quad (4.9)$$

At lower energies up to hundreds of keV, the photoelectric effect dominates, followed by Compton scattering in the MeV range until the GeV range where electron/positron pair production dominates.

4.2.4 Hadrons

Hadrons are composite particles made of quarks, antiquarks and gluons. Not only can they interact electromagnetically via processes described in earlier sections, but they can also interact via the strong force in inelastic collisions to create secondary particles. The absorption of hadrons can be described by the exponential decrease of the number of hadrons in a beam with an initial number of hadrons of N_0 when going through a length x of absorber material [19]:

$$N(x) = N_0 e^{-x/\lambda_I} \quad (4.10)$$

Where:

λ_I : nuclear interaction length depending on the cross section of inelastic collision in the absorber material and its density. This is the mean path length traveled by a beam of hadrons to reduce its number of particles by a factor $\frac{1}{e}$. In general, $\lambda_I \gg X_0$ for most materials.

4.3 Showers

As mentioned above, the particles of special interest all produce secondary particles with the exception of the muons. In turn, these secondary particles can also be expected to produce more particles and so on. The phenomenon where multiple interactions couple together to cause a cascade of particle production processes is referred to as a particle shower.

The reconstruction of an event in a particle accelerator depends on the quality of the energy deposition measurements of the particle showers occurring in the calorimeters.

Accurate measurements are possible if most of a shower is contained by the calorimeter, thus a calorimeter's dimensions are dictated by the type and shape of the particle showers it must optimally measure. Knowledge of shower physics presented in this section lets physicists predict the width and depth of calorimeters needed to study a broad range of energy.

4.3.1 Electromagnetic Shower

At energies higher than 1 GeV, Bremsstrahlung is the main energy loss process for electrons and positrons while it is pair production for photons. Consequently, incoming photons and electrons will create secondary particles as they traverse the detector medium, releasing photons and electrons. These latter also undergo Bremsstrahlung and pair production, releasing more electrons and photons. This shower of secondary

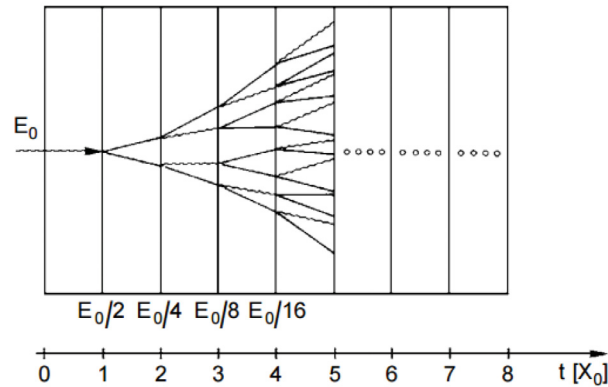


FIGURE 4.3: Schematic of an electromagnetic shower longitudinal profile traversing many radiation lengths X_0 of an absorber. The initial energy E_0 gets attenuated by half at every X_0 traveled [19].

particles will run its course and degrade particle energy until they reach a critical energy E_c where ionization dominates energy losses for electrons and photoelectric effect or Compton scattering for photons. A profile of such a shower is found in Figure 4.3. In fact, the shower stops when its remaining energy is not sufficient to create more secondary particles.

The mean penetrating depth distribution of an electromagnetic shower can be approximated by [14]:

$$\frac{dE}{dx} = E_0 b \left(\frac{(bt)^{a-1} e^{-bt}}{\Gamma(a)} \right) \quad (4.11)$$

Where:

a, b : parameters related to the incident particle (electron(positron) or photon)

t : material depth in radiation lengths

The depth t_{max} at which the largest number of particles are generated is approximately:

$$t_{max} \approx \ln \left(\frac{E_0}{E_c} \right) + t_0 \quad (4.12)$$

Where:

$t_0 = -0.5(+0.5)$ for electrons(photons)

E_c : critical energy of the charged particles in the beam. The critical energy is the energy at which the losses incurred by ionization are equal to the ones due to Bremsstrahlung radiation where $E_c \approx \frac{750}{Z}$ [MeV] [22].

The shower lateral size is due to the dispersion of secondary electrons and photons away from the shower central axis due to collisions with the detector matter. The Molière radius R_M corresponding to the average lateral dispersion of the electrons at E_c after traveling one radiation length X_0 offers a good approximation [14]:

$$R_M \left(\frac{g}{cm^2} \right) \approx 21 MeV \left(\frac{X_0}{E_c (MeV)} \right) \quad (4.13)$$

In practice, a good rule of thumb is that a cylinder of radius of $2 R_M$ and principal axis corresponding to the shower axis contains 95% of the shower energy.

4.3.2 Hadronic Shower

Hadronic showers are less well understood than their electromagnetic counterparts because of the complexity and probabilistic nature of the different mechanisms involved. In general, energetic hadrons traveling through a detector material will interact strongly by producing more hadrons which in turn will produce more and so on.

These secondary hadrons are mainly pions and nucleons. They will travel a mean free path λ before interacting with matter which translates into a more penetrating shower than an electromagnetic one at the same energy [19]:

$$t_{max}(E) \approx 0.2 \ln E_0 [GeV] + 0.7 \quad (4.14)$$

Also, hadronic showers are more laterally spread out because of the high transverse momentum of the secondary hadrons. Effectively, 95% of an hadronic shower is contained within a cylinder of radius λ [19].

The frequent generation of π^0 which decays into two energetic photons adds an electromagnetic component to the shower. This component grows with the energy. Large energy fluctuation and the possibility of a dominant electromagnetic component make the detection of hadron shower a challenge when it comes to high energy resolution.

Additionally, the fact that some of the hadronic shower energy remains invisible to detection due to the nature of the energy loss (nuclear binding, fission, spallation...) also impacts the energy resolution. As a general rule, the ratio of the response of a calorimeter to an electron or hadron, $\frac{e}{h}$, is always larger than one because of this invisible energy. It is possible to use compensating calorimeters to reduce this effect by using a software approach or a hardware approach. For example, the ZEUS experiment achieved $\frac{e}{h} = 1$ by using uranium as an absorber [20].

4.4 Energy Resolution

The measurement of energy in a detector is based on the principle that the incident particle energy is proportional to the total energy deposited in the active region of a detector through all the energy loss processes occurring during the particle shower. Energy resolution $\frac{\sigma_E}{E}$ takes the general form [14]:

$$\frac{\sigma_E}{E} = \frac{a}{\sqrt{E}} \oplus \frac{b}{E} \oplus c \quad (4.15)$$

Where:

a: stochastic term which depends on the event by event energy fluctuations in the energy depositions.

b: noise term due to the readout electronics and detector technology and is energy dependent.

c: constant term which is independent of the incident particle energy. It encapsulate effects due to instrumentation defects, detector geometry among others.

\oplus : quadratic sum operation

The presence of other limiting factors such as lateral and longitudinal energy leakage in the detector and upstream energy loss are worth mentioning. Generally, the

stochastic term limits hadronic shower energy resolution because of the invisible energy mentioned in Section 4.3 which spreads the distribution of event-by-event energy fluctuations.

Chapter 5

Calorimetry and CALICE Detectors

The Calorimeter for Linear Collider Experiment collaboration or CALICE collaboration, is an international group of physicists and engineers researching and developing new detector technologies to be used in future electron/positron accelerators functioning at the TeV scale for applications in different fields whether it be medicine, particle physics or any others. In particular, the group is developing new sampling calorimeters with PFA in mind. Prototypes of different calorimeter technologies have been built. This chapter introduces the three main prototypes with an emphasis on the DHCAL which is the subject of this thesis.

5.1 Calorimetry

Calorimetry encompasses the science and the detection techniques of measuring the energy of an incoming particle. Ideally, the detector matter would be sufficient to stop the particle completely, thus, collecting all the energy depositions that occurred along the travel path length. In practice, detectors built for this sole purpose, the calorimeters, are usually made of a sequence of active layers where physical readings occur and absorber layers made of a higher density material where incoming particles are slowed down. This is the case for sampling calorimeters. The homogeneous calorimeter is another type of calorimeter where one material plays the role of absorber and active layer at the same time.

5.1.1 Homogeneous Calorimeter

Just as its name suggests, the homogeneous calorimeter is made of one material which acts both as absorber to slow down particles, and active layer to collect the energy deposition.

The energy resolution is generally good because most of the incoming particles energy is deposited in the detector. Also, the energy fluctuations are minimal event by event.

The difficulty to segment the detector limits its spatial resolution. In addition, the materials used for this type of calorimeter have large interaction lengths which makes it extremely difficult to build reasonably sized detectors to contain hadronic showers. Furthermore, an increase in size also means an increase in material cost and electronic read-out complexity. The latter can affect the calorimeter response by heating up the active material thus artificially changing the gain for example. Also, larger sizes mean non-uniform time responses.

5.1.2 Sampling Calorimeter

In contrast to the homogeneous calorimeter, the sampling calorimeter is segmented into a sequence of absorber layers made of dense material to slow down the incoming particles and active layers which record the energy loss.

The energy resolution is usually worse than the homogeneous calorimeter because of segmentation fluctuations and the fact that only a fraction of the total energy is measured since a good fraction of the energy is lost in the absorber layers. However, a better spatial resolution can be achieved more readily with sampling calorimeters by segmenting the active layers into more sampling units. In other words, increasing the granularity of the active layers is equivalent to creating more mesh in the spatial grid of the detector thus improving the spatial resolution.

Also, the presence of absorber layers means that a smaller sampling calorimeter can contain a high energy shower. Effectively, less sampling calorimeter depth is needed to stop a high energy particle than it would be the case for a homogeneous calorimeter. The calorimeters developed by the CALICE collaboration and discussed in this thesis are all sampling calorimeters.

5.2 AHCAL

The Analog Hadron Calorimeter (AHCAL) is a design alternative for the ILC calorimeters developed by the CALICE collaboration. A prototype of the AHCAL was built and tested during the years 2006 to 2010 at CERN, DESY and Fermilab [13].

5.2.1 Overview of the Prototype

The prototype has 38 layers of active medium. One layer consists of the succession of a 2 cm thick steel absorber and a 0.5 cm thick plate of plastic scintillator tiles which vary in lateral sizes. Tile size comes in $3 \times 3 \text{ cm}^2$ in the inner region, $6 \times 6 \text{ cm}^2$ and $12 \times 12 \text{ cm}^2$ at the outer region. In total, 7608 plates are used in the prototype.

In turn, these plates are coupled to Silicon Photomultipliers (SiPM) via wavelength shifting fibers. When an energetic particle travels within the scintillator material, light is produced by excitation. The photomultipliers collect the charge which is proportional to the total energy of the particle, and amplify the signal with a known gain. The SiPMs are built with avalanche photodiode (APD) arrays on silicon. One photon causes an avalanche of charges which produces a macro signal in the mA range which can be collected by electronics [13].

5.2.2 Strengths and Weaknesses

Test beams involving muons, pions and electrons/positrons beams or a mixture of the three with energies between 1 to 180 GeV were used. The response in pion energy was noted to be non-linear because of the intrinsic non-compensating nature of the AHCAL [10].

Despite this difficulty, the energy calibration using the emitted light by MIP as a unit of energy into total energy in GeV yielded an improved stochastic term for pions of $\sim \frac{45\%}{\sqrt{E \text{ (GeV)}}}$ using compensating software techniques compared to $\sim \frac{58\%}{\sqrt{E \text{ (GeV)}}}$ before calibration. The constant term was estimated to be 1.6% [10].

5.3 SDHCAL

The Semi Digital Hadron Calorimeter (SDHCAL) is a second alternative design for the ILC calorimeters that the CALICE collaboration is researching. A prototype was built in 2011 and tested at CERN in 2012 [11].

5.3.1 Overview of the Prototype

The prototype has 48 layers. One layer consists of 1×1 m glass RPC (GRPC). The GRPCs signal is read by 9216 1×1 cm² pickup pads located on one face of electronics boards while the other face holds 144 Hadronic RPC Digital Calorimeter Read-Out Chips (HARDROCs) application-specific integrated circuits (ASICs). These ASICs have 64 channels with 3-threshold readout [11].

One active layer is put inside a cassette made of two 2.5 mm thick stainless steel. One absorber layer is made of 1.5 cm thickness stainless steel plate corresponding to approximately 0.12 interaction lengths or 1.14 radiation lengths in total [11]. The absorber layers are 13 mm apart and are part of the structure that holds the cassettes.

The specificity of the SDHCAL lies in the multi-threshold used to read the signal coming from the GRPCs. With the 3-threshold readout, the electronics is able to discriminate between pads where few, many or a large number of charged particles crossed the GRPCs [11].

5.3.2 Strengths and Weaknesses

In general, digital calorimeters will have a faster readout than analog ones because they do not need to convert any analog signal to a digital one. The lack of Analog to Digital Converter (ADC) also lowers the cost of the digital calorimeter.

During the tests performed at CERN, the multi-threshold offered a better energy resolution for multi-threshold at $E > 30$ GeV than one threshold only. It reduced the fake MIPs events such as two particles incident on the same pad, separated by a larger distance than avalanche size which would lead to the addition of their charge. In turn,

this charge would be attributed to a single particle of higher energy if it were not for the multi-threshold[11].

On the other hand, the multi-threshold complexifies the readout structure and electronics leading to an increase of electronic noise. In addition, the heating derived from the electronics was observed to influence the neighboring RPCs by changing their gain and decreasing their efficiency over time[11]. The use of a water cooling system is considered as a solution to this problem.

5.4 DHCAL

The Digital Hadron Calorimeter (DHCAL) prototype was built in 2009 and underwent testing at CERN and Fermilab during the two following years. This calorimeter is the last one developed by the CALICE collaboration in the context of the ILC. It is also the subject of this thesis.

5.4.1 Overview of the Prototype

Similarly to the SDHCAL, the active medium of the DHCAL are $1 \times 1 \text{ cm}^2$ GRPCs readout pads or cells necessitating 480,000 readout channels. Unlike the SDHCAL multi-threshold, one pad has a resolution of one bit. Once a pad records a signal above the 1-bit threshold, the signal is picked up by the embedded front-end electronics, then it is processed by the back-end electronics before entering the Data Acquisition (DAQ) system which converts it into digital data recorded by a computer.

One active layer of the DHCAL is roughly $1 \times 1 \text{ m}^2$, hosting three GRPCs, each of dimension 96×32 cells. Figure 5.1 illustrates the GRPC configuration of the first layer which is identical to all layers. Two front-end electronics boards, each of dimension $32 \times 48 \text{ cm}^2$, span a GRPC. Each board holds 24 ASICs. Such a configuration impacts the data recorded by the DHCAL prototype by creating preferred track angles. Indeed, if the prototype's principal axis, which is perpendicular to the layers, is taken to be the Z-axis (Figure 5.2), then the geometric configuration of the pads into a grid in the XY-plane favors tracks with zenith angle of 0° , 90° , 180° and 270° and azimuthal angle of 0° and 90° .

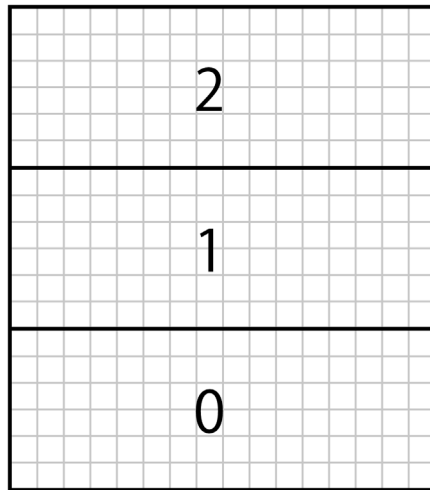


FIGURE 5.1: RPC configuration of the first layer (not to scale). The bottom layer is labeled RPC 0, the middle layer RPC 1 and the top layer RPC 2.

Also, the distance between two cells facing each other on two consecutive layers is 3.17 cm [2] while the center-to-center distance between any two neighboring cells on the same layer is 1 cm.

Grounding problems were discovered at the edges of a layer resulting in an increase of fake hits[16]. Similarly, a higher density of hits was systematically observed at the GRPCs borders. Figure 5.3 shows an event from a run at 60 GeV displaying a grounding problem at the middle RPC's borders. Such events are discarded during event selection (Chapter 5).

5.4.2 Technical details and Fermilab Configuration

This thesis analyzes the data that was taken with the DHCAL in the 2011 Fermilab configuration where the main stack consisted of a 38-layer structure with 17.4 mm thick steel absorber plates between layers[2].

The main stack was mounted on a movable stage enabling lateral and vertical motion as well as rotation about the vertical axis. As mentioned earlier, the layer-to-layer distance was 3.17 cm. In total, the main stack had a thickness of 48.6 radiation lengths or 5.23 interaction lengths[2].

Another 14-layer structure with 2.0 cm thick steel plates followed by six 10.0 cm thick

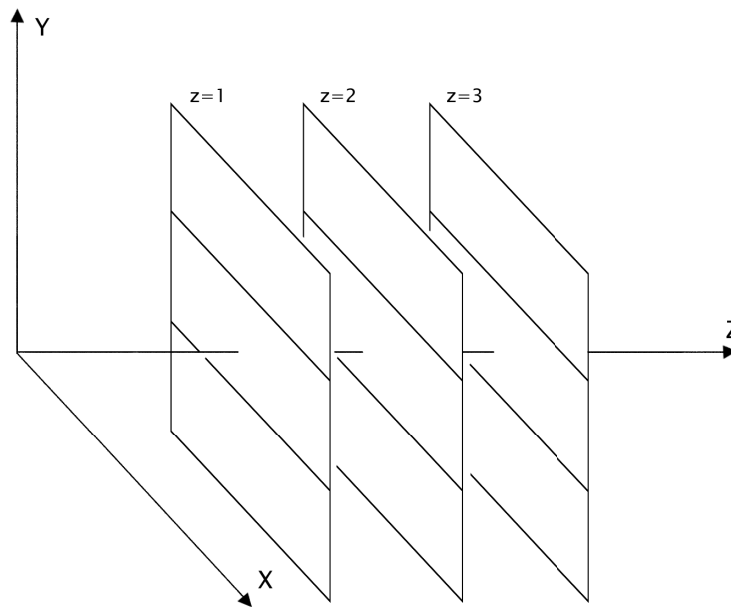


FIGURE 5.2: Principal axes of the DHCAL. The layers are perpendicular to the Z-axis.

steel plates was used in addition to the DHCAL, the Tail Catcher and Muon Tracker (TCMT). This structure was positioned directly after the prototype to record the tail of hadronic and electromagnetic showers and further muon track recordings.

During the same period, another configuration without absorber layers, the Min-DHCAL, was studied at lower energy runs[16]. The absence of absorber layers enabled the hadronic showers to propagate more deeply in the calorimeter thus improving the energy and spatial resolution at low energies, thus providing invaluable data on low energy showers.

5.4.3 Energies and Data Format

The data of interest in this thesis are the DHCAL test beam runs taken during June 2011 at Fermilab. These test beams occurred in triggered data taking mode. Generally, hit patterns in 7 time bins (1 bin is 100 ns long) were recorded. The beam contained pions, electron and muons when it was not a dedicated muon-only run. The energies spanned by these selected runs are 32 GeV, 40 GeV, 50 GeV, 60 GeV, 120 GeV for normal test beams. Some runs were recorded at 8 GeV, 16 GeV and 32 GeV with the main stack rotated by 10° about the vertical axis.

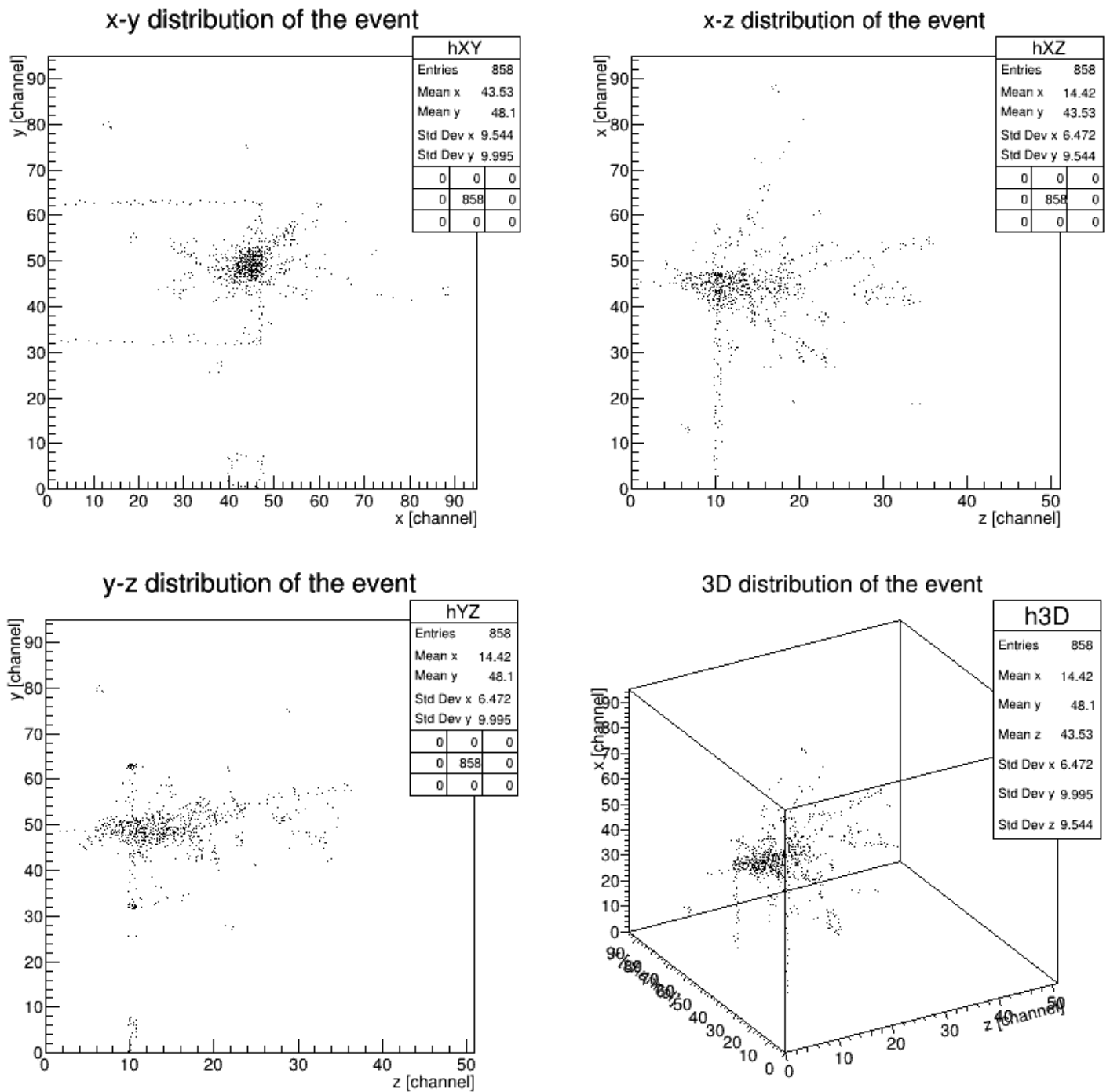


FIGURE 5.3: Example of grounding problems in layer $z = 10$ at a GRPC bottom and top borders for a run at 60 GeV. The four graphs are the projections of a 3-dimensional event hit distributions.

The data from one run takes the form of a text file with 4 columns, recording the time stamp of a hit and the x -, y -, z -coordinates of said hit in the main stack and TCMT. The three coordinates correspond to the position of the pad that registered the hit. An event starts with a time stamp and a header where $x = -1$, $y = 0$ and $z = -1$ before its hits are listed.

5.4.4 Strengths and Weaknesses

The DHCAL GRPC technology is considerably cheaper than the SiPMs used in the AHCAL[2].

Unlike the AHCAL, digital saturation effects are more likely to occur in the DHCAL due to counting the number of hits instead of measuring actual energy deposition. This lowers the energy resolution at higher energies. The SDHCAL approach palliates this issue with the multi-threshold[8].

The readout is less complex than in the SDHCAL, lessening the temperature impact on the GRPCs and probably offering a cheaper alternative to the SDHCAL which will probably need the addition of a water cooling system. These observations are not negligible when considering the large calorimeter detector volume required by the ILC. Also, the lack of analog to digital converter makes the readout faster than the AHCAL's and lowers the cost of manufacturing.

Chapter 6

Event Selection

6.1 Faulty Events and the Associated Cuts

The raw data needs to undergo quality cuts to ensure that it corresponds to physical phenomena and not faults in the electronics. In addition to these cuts, more cuts are applied to keep only single entry events that started their shower within the DHCAL main stack like the 40 GeV pion event in Figure 6.1. This selection and the following particle identification are performed by a program created at McGill University in 2013[25] specifically for the DHCAL which continued to undergo development[16] until now.

Figure 6.2 is a 40 GeV run summary where the main statistics of all its events without any cuts applied, are compiled. The run profiles in the x-y, x-z and y-z planes make it possible to tell if a run has a normal spatial distribution. For example, these profiles illustrate the normal propagation of the beam within the calorimeter with the exception of a dead RPC at $z = 19$ (k), some grounding problems along $x = 0$ (k) and some cells that are always firing along $y = 52$ and $y = 84$. Also, a decrease in the number of hits close to RPC borders which appear as white strips along $y = 32$ and $y = 64$ in the y-z and x-y planes can be noted. Plots (v) to (x) confirm that the beam was fired in the center of the calorimeter as most hits in the x- and y-planes are recorded mid-detector and that the beam contained the most of the run as less events are recorded with hits at the end of the main stack at $z = 37$ (x). The plots from (a) to (i) are scatter plots of the identification parameters listed in Section 6.2 vs the number of hits. The expected correlations of these parameters with the number of hits discussed in Section 6.2 are used to define the particle identification cuts which are obvious in (a), (b) and (c) thanks to the color code. Plots (p) to (u) describe the average profiles of all particle

showers recorded by plotting the number of events versus various shower statistics. For example, a typical event of this run has ~ 600 hits (p), traverses 10 layers (q, r, t) and has a maximum width of 20 cm (s).

6.1.1 Too Few Hits and Too Many Hits

Events with less than 10 hits are discarded since they are most likely due to a fake signal or electronic noise. Similarly, events with more than 4000 hits are discarded.

6.1.2 Faulty Layer

A faulty layer event exhibits an abnormal illumination in one or more of its RPCs as Figure 6.3 illustrates. All layers are divided into six equal regions, two per RPCs, corresponding to the electronic ASIC units. The number of hits in each region is compared to neighboring regions. If the number of hits in the tested region is > 15 hits and the difference in the number of hits between the two regions is larger than a factor 1.2, the corresponding layer is identified as faulty.

6.1.3 Early Showering

Some events are the results of particle showers that started upstream as illustrated by Figure 6.4. To ensure a good quality for the calibration and particle identification, only showers starting within the calorimeter are kept since they deposited most of their energy within the calorimeter. If the last reached layer reached by an event is within the first three layers, it is discarded. If the number of hits recorded in the first layer or second layer is higher than 2.5 times the average number of hits per layers traversed during an event, this event is also discarded.

6.1.4 Multiple Entries

For ease of analysis, only single incoming particle events are kept. Therefore, events similar to the one displayed in Figure 6.5 are discarded. To do so, the two regions with

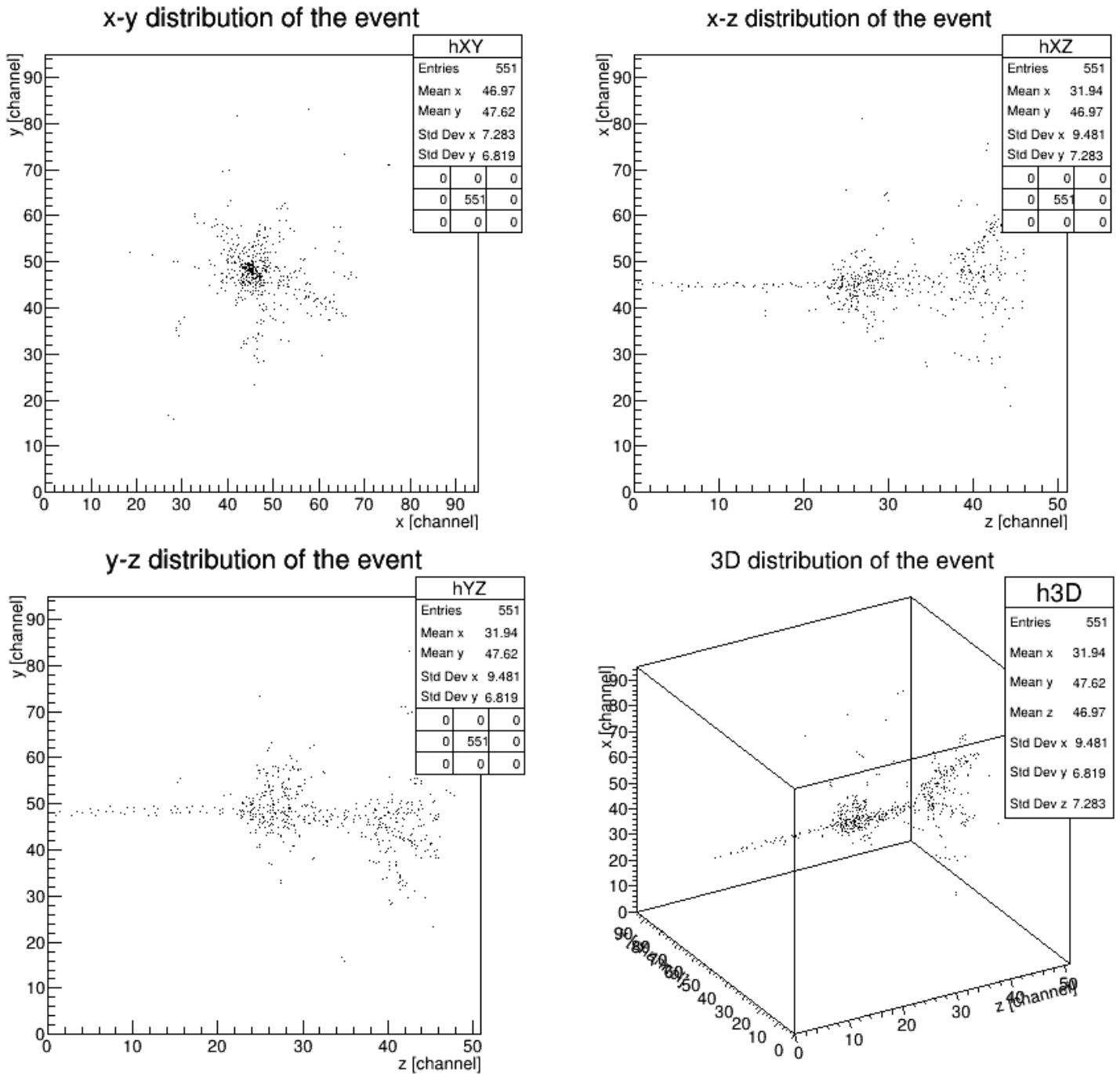


FIGURE 6.1: Projections of a 3-dimensional good single pion event at 40 GeV. The initial MIP track is exceptionally visible in the x-z and y-z profiles as well as the tracks from secondary particles coming from the interaction core.

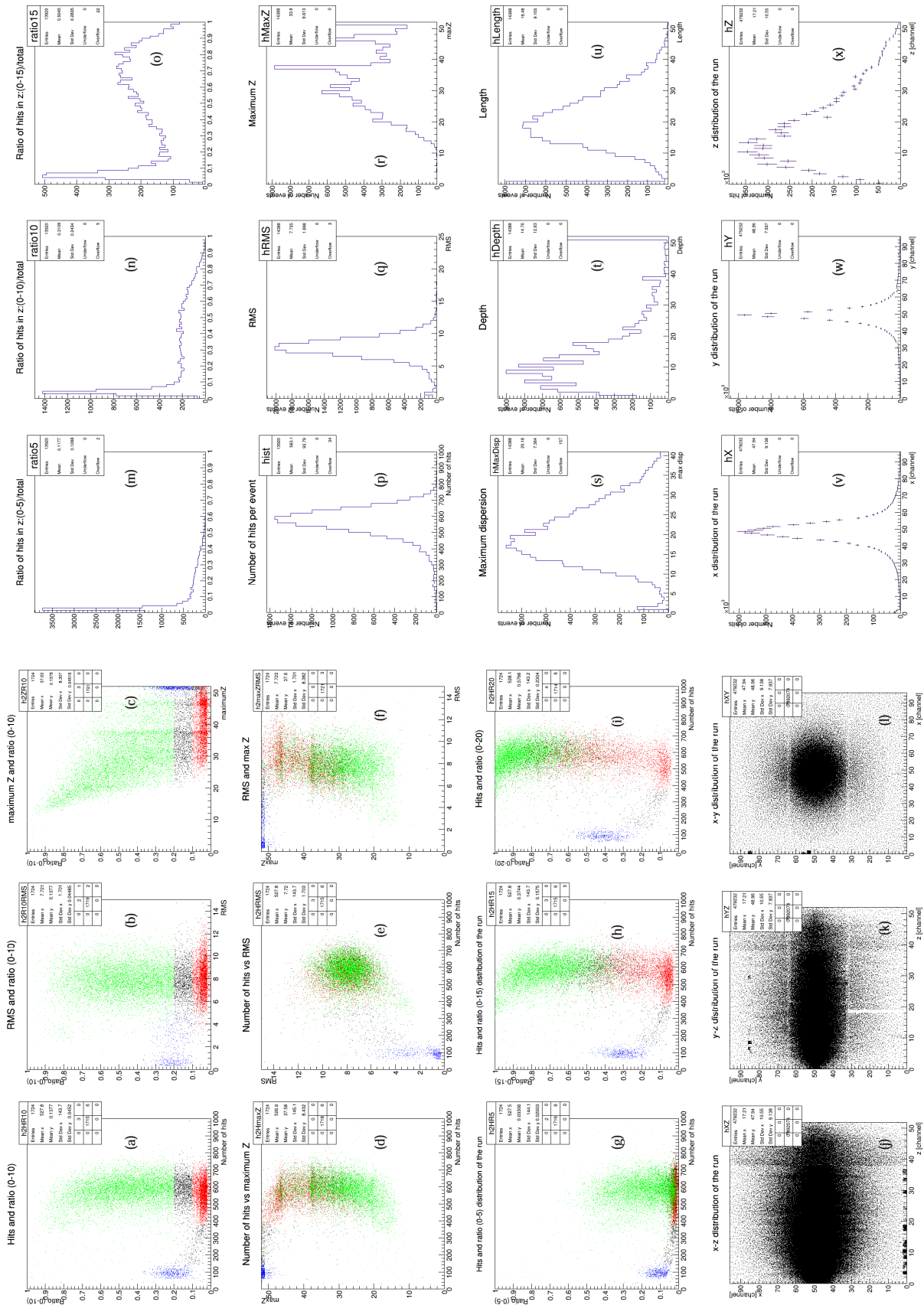


FIGURE 6.2: Run summary of all the 18,954 events (no cut) from a 40 GeV run. Pion identified events are red, electron identified events are green, muon identified events are blue and the remaining black events are undetermined.

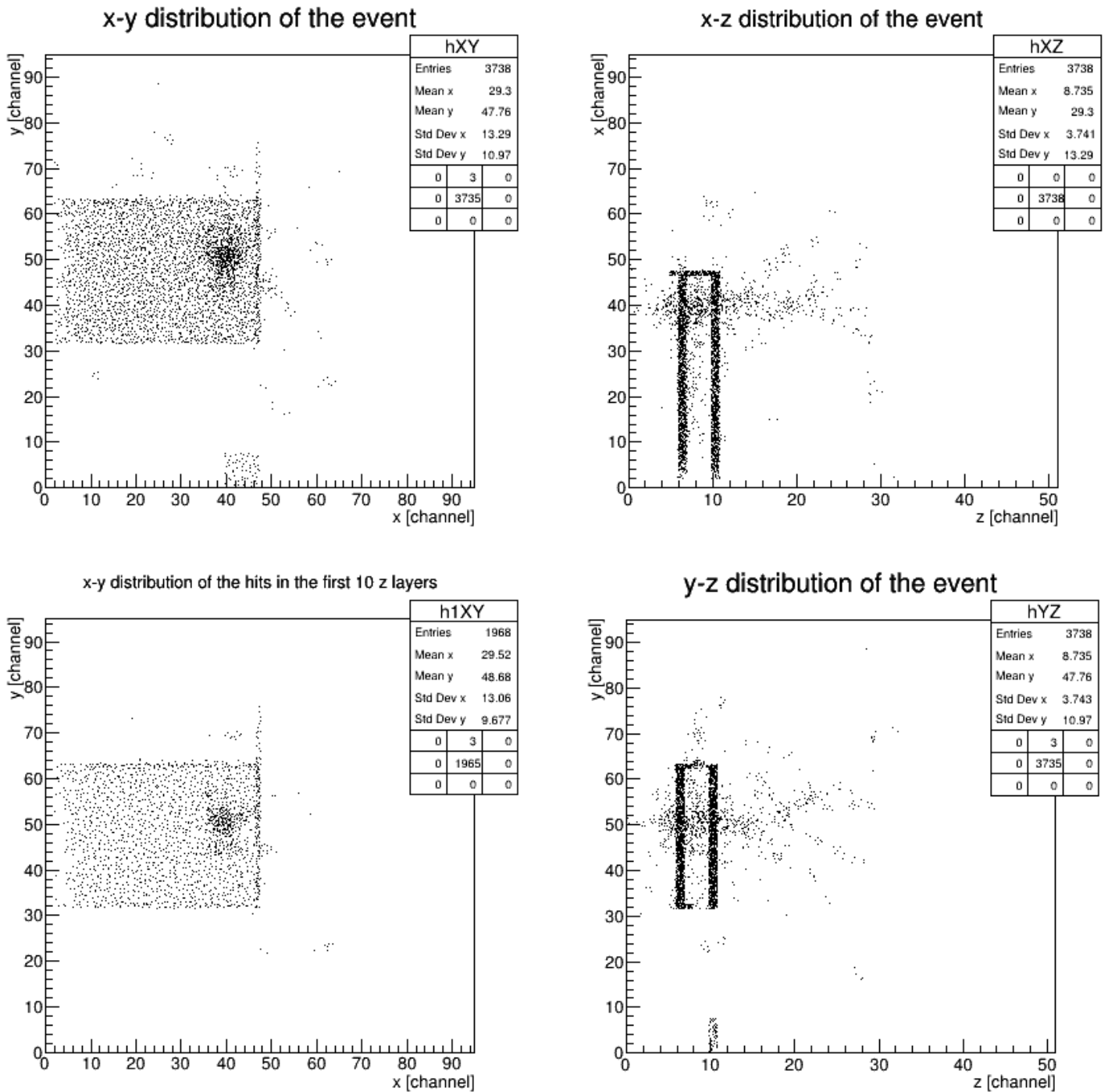


FIGURE 6.3: Example of a faulty layer event during a run at 60 GeV. The four graphs are the projections of the 3D event. The layers $z = 6$ and $z = 10$ have their middle RPC illuminated in their entirety during an event. Some abnormal illumination can also be noted in layer $z = 10$ in the bottom RPC where $y \in [0, 8]$.

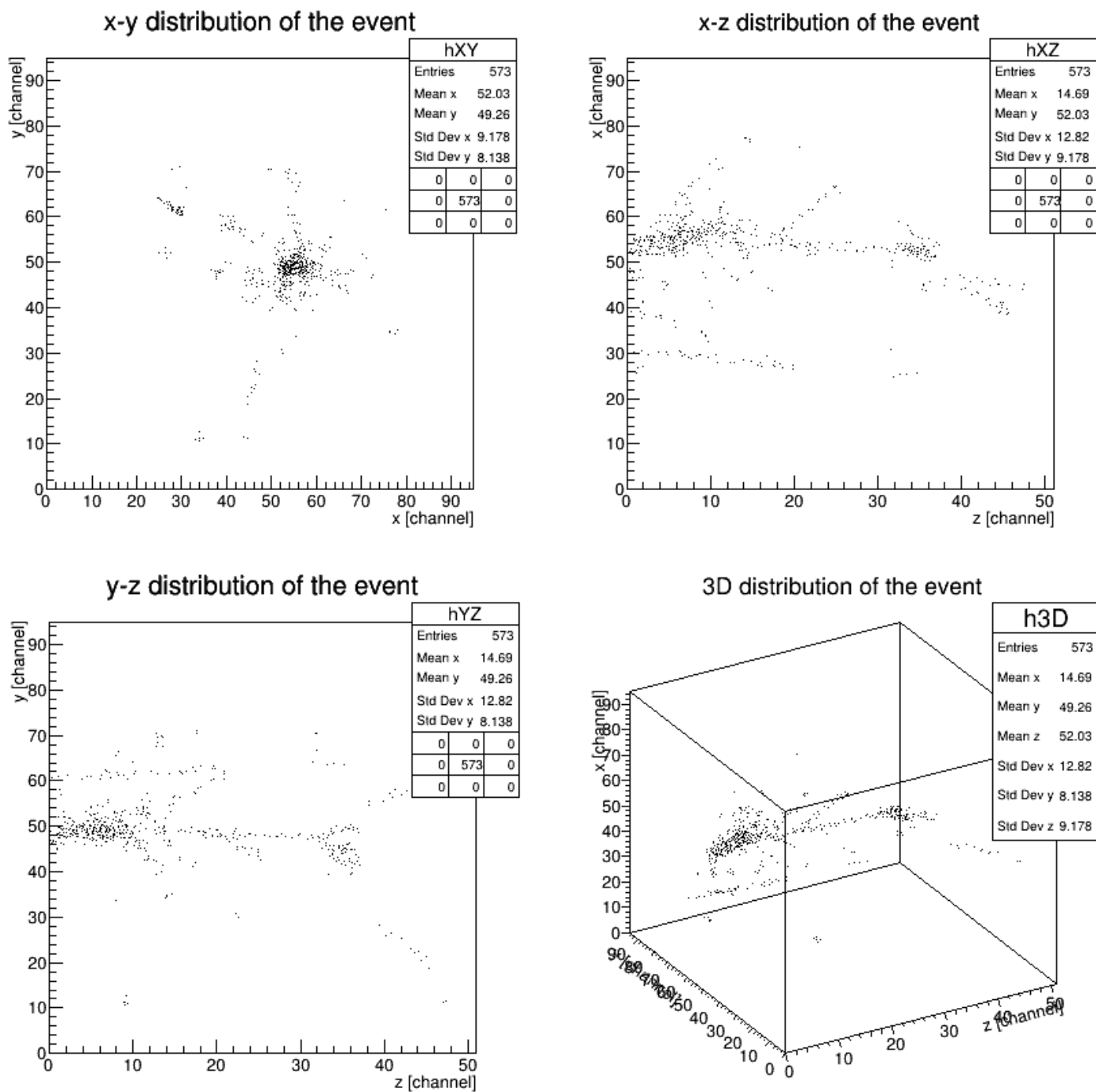


FIGURE 6.4: Projections of a discarded multi-entry event that started upstream during a run at 50 GeV. Two points of entry can be identified at $(x=30, y=60)$ and $(x=48, y=49)$. The first one seems to belong to a muon as its linear track within the DHCAL suggests. The second one belongs to a pion that started interacting with detector matter upstream as the lack of an initial track implies.

the highest hit densities within a same layer are found. If one region has a hit density higher than 20% of the other one's, the event is discarded.

6.2 Surviving Events and Particle Identification

The surviving events are then matched as well as possible to a particle type (muon, pion, electron/positron or undetermined). The particle type is determined by constraining values of specific parameters.

6.2.1 Identification Parameters

These parameters, based on distributions like Figure 6.2 for each data run, are computed for each identified event of a run:

ratio5 Ratio of hits in the first 5 layers to the total number of hits.

ratio10 Ratio of hits in the first 10 layers to the total number of hits.

ratio15 ratio of hits in the first 15 layers to the total number of hits.

numHits Number of hits in the event.

RMS Root Mean Square of the event hit distribution in the x-y plane.

maxZ Maximum Z layer reached by the event

length Length of the shower excluding the MIP entry track.

maxDisp Maximum dispersion reached in a Z layer.

The hits in an event can be likened to a cloud of hits. By fitting this cloud of hits to a paraboloid, it is possible to fit its main axis to a line. The dispersion is defined as the distance of a hit to this fitted main axis. **maxDisp** is the maximal distance reached by a hit recorded in a layer Z from the fitted main axis .

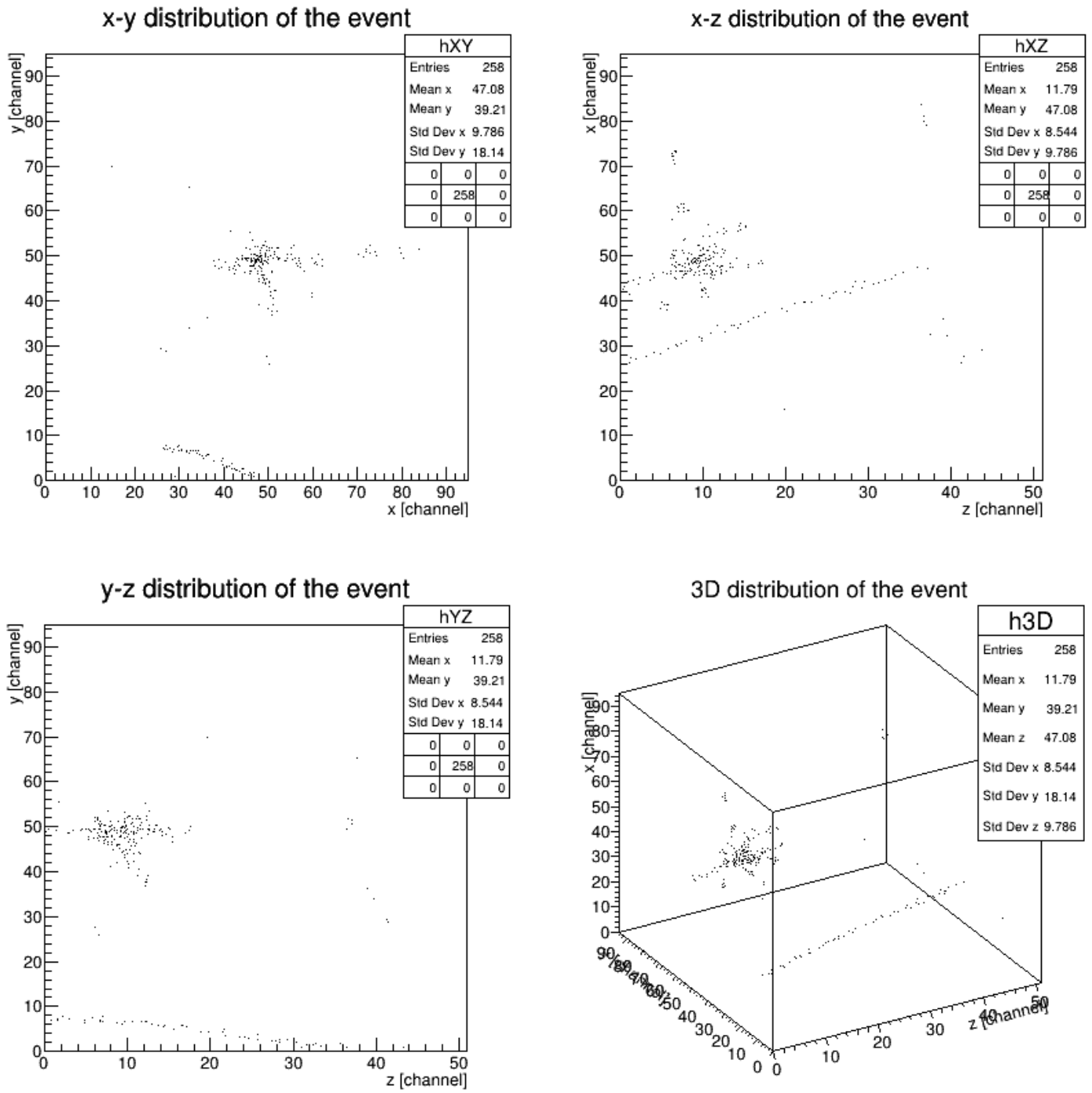


FIGURE 6.5: Projections and 3D view of a multiple entries event involving a muon during a run at 16 GeV. The muon track starting at $(x=30, y=8)$ is especially visible in the x-z projection and 3D view.

Parameter	8 GeV	16 GeV	32 GeV	40 GeV	50 GeV	60 GeV	120 GeV
ratio10	< 0.3	< 0.2	< 0.2	< 0.1	< 0.1	< 0.1	< 0.1
numHits (hits)	> 50	> 150	> 300	> 400	> 500	> 600	> 1000

TABLE 6.1: Principal constraints on the identification parameters to match an event to a pion for different energies of a run.

6.2.2 Muons

Muons are perceived as MIPs in the calorimeter which means that their energy deposition is independent of their incoming energy. This results in long linear tracks in the detectors just like in Figure 6.6 at all energies. Therefore, a small ratio10 ($\in [0.05, 0.45]$) and ratio15, a relatively small number of hits (< 150) compared to electrons and pions, as well as a small RMS (< 8) and maxDisp (< 15) are expected from a muon event for all energies.

6.2.3 Pions

Pions travel into the first layers of the detector before interacting with matter and starting a hadronic shower as illustrated by Figure 6.7. The interaction length in the first layers and the shape of the shower depend on the energy of the incoming pions, hence, the parameters for pion identification must vary with energy. Pions have a longer initial track than electrons which means that for the same energy, their ratio5 and ratio10 will generally be smaller. To be identified as a pion event, an event must obey all the conditions listed in Table 6.1 for its specific energy.

6.2.4 Electrons/Positrons

Electrons have a shorter initial track than pions of the same energy. Also, their electromagnetic showers are narrower than the pions' for the same energy. Again, the shape of the electromagnetic shower generated by an electron event depends on the incoming energy of the latter. Figure 6.8 shows an example of an electron event where the MIP entry track is restricted to the first 3 layers of the detector. To be identified as an electron event, an event must obey all the conditions listed in Table 6.2 for its specific energy.

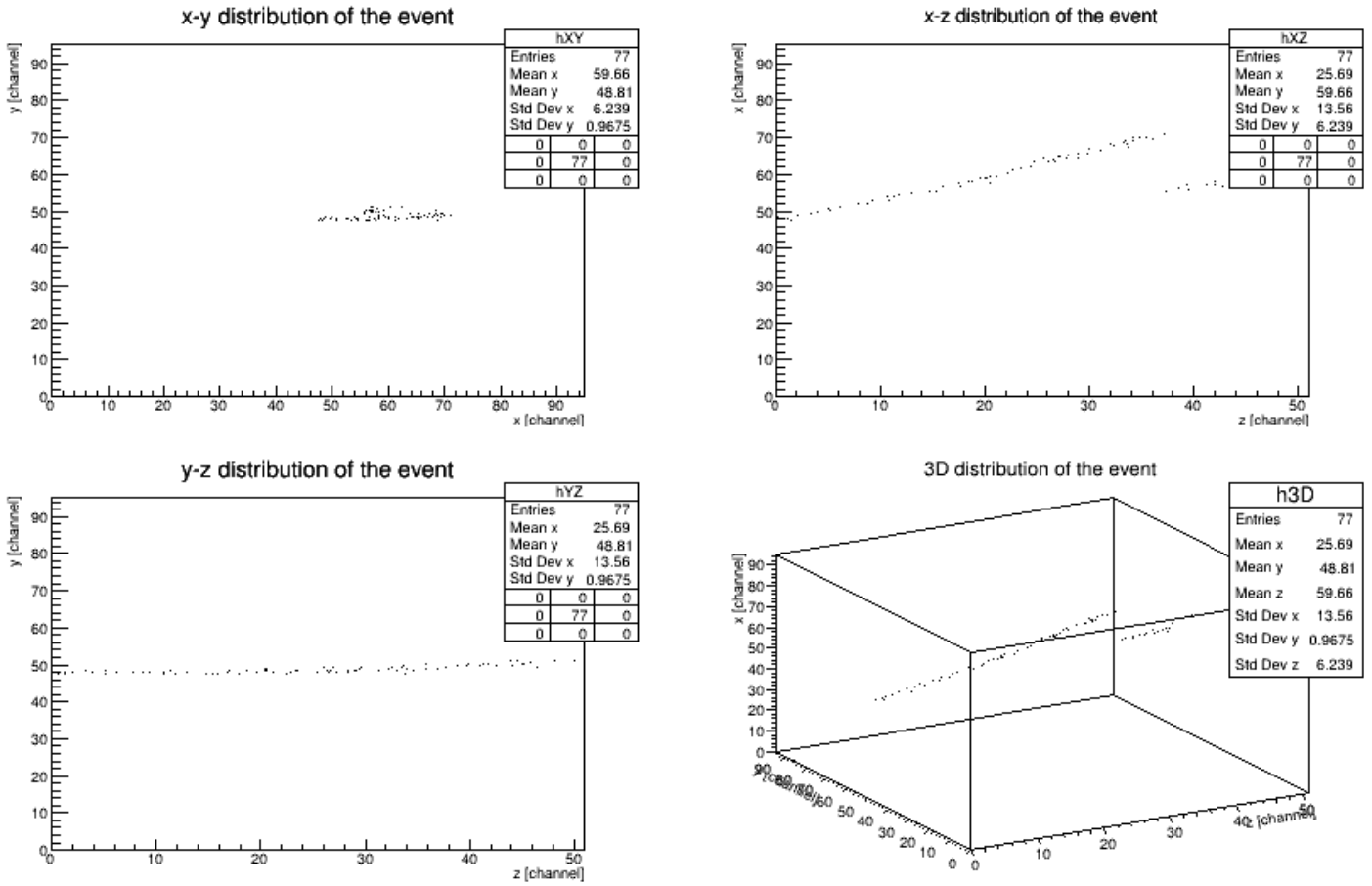


FIGURE 6.6: Projections and 3D view of a muon event from a 32 GeV run where the DHCAL was rotated by 10° . Note that the tracks where $Z > 37$ were recorded by the TCMT and were excluded from the analysis presented in this thesis.

Parameter	8 GeV	16 GeV	32 GeV	40 GeV	50 GeV	60 GeV	120 GeV
ratio10	> 0.4	> 0.3	> 0.3	> 0.2	> 0.2	> 0.2	> 0.2
numHits (hits)	> 50	> 150	> 300	> 400	> 500	> 600	> 1000

TABLE 6.2: Principal constraints on the identification parameters to match an event to an electron for different energies of a run.

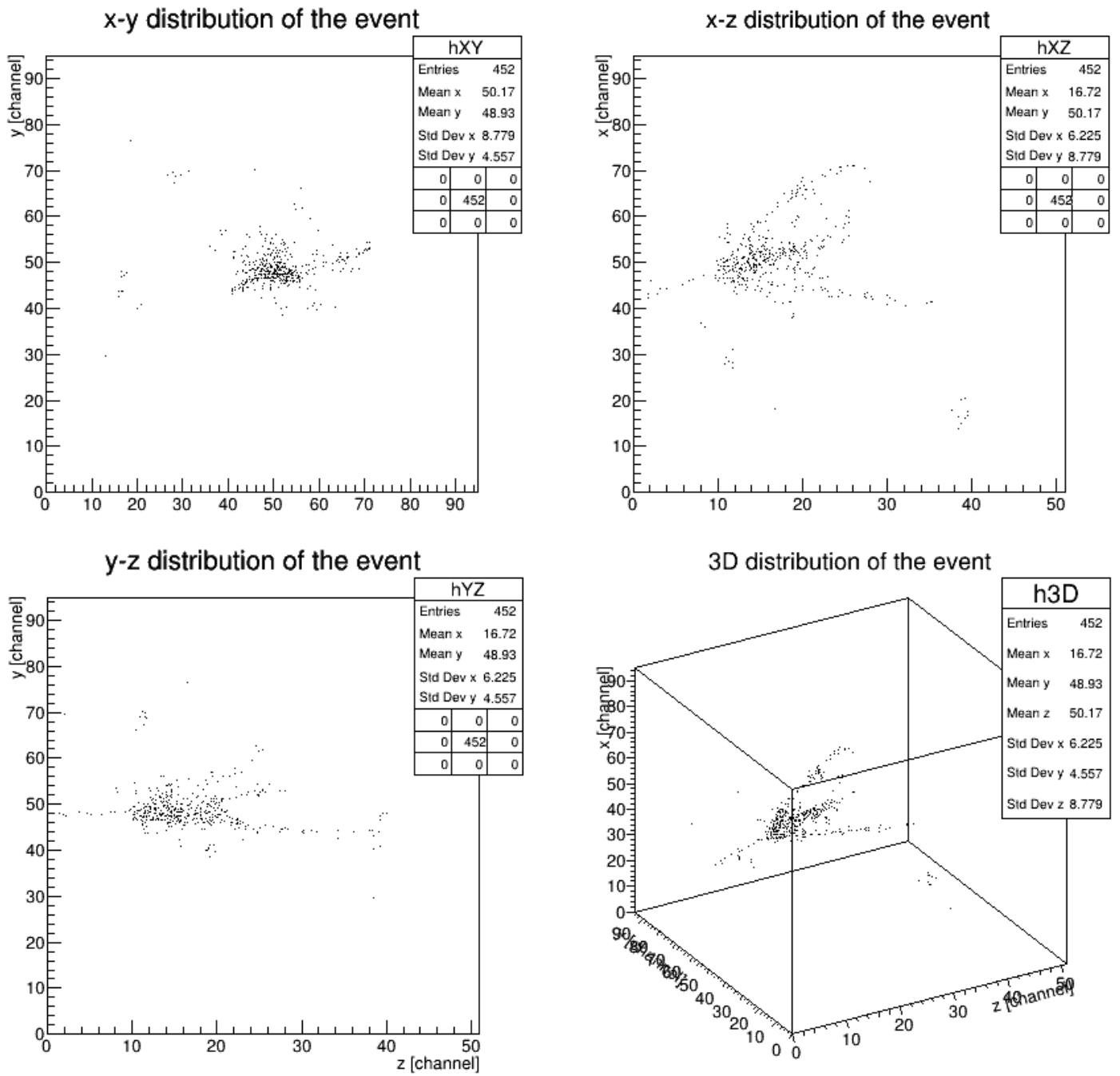


FIGURE 6.7: Projection and 3D view of a pion event from a 32 GeV run.

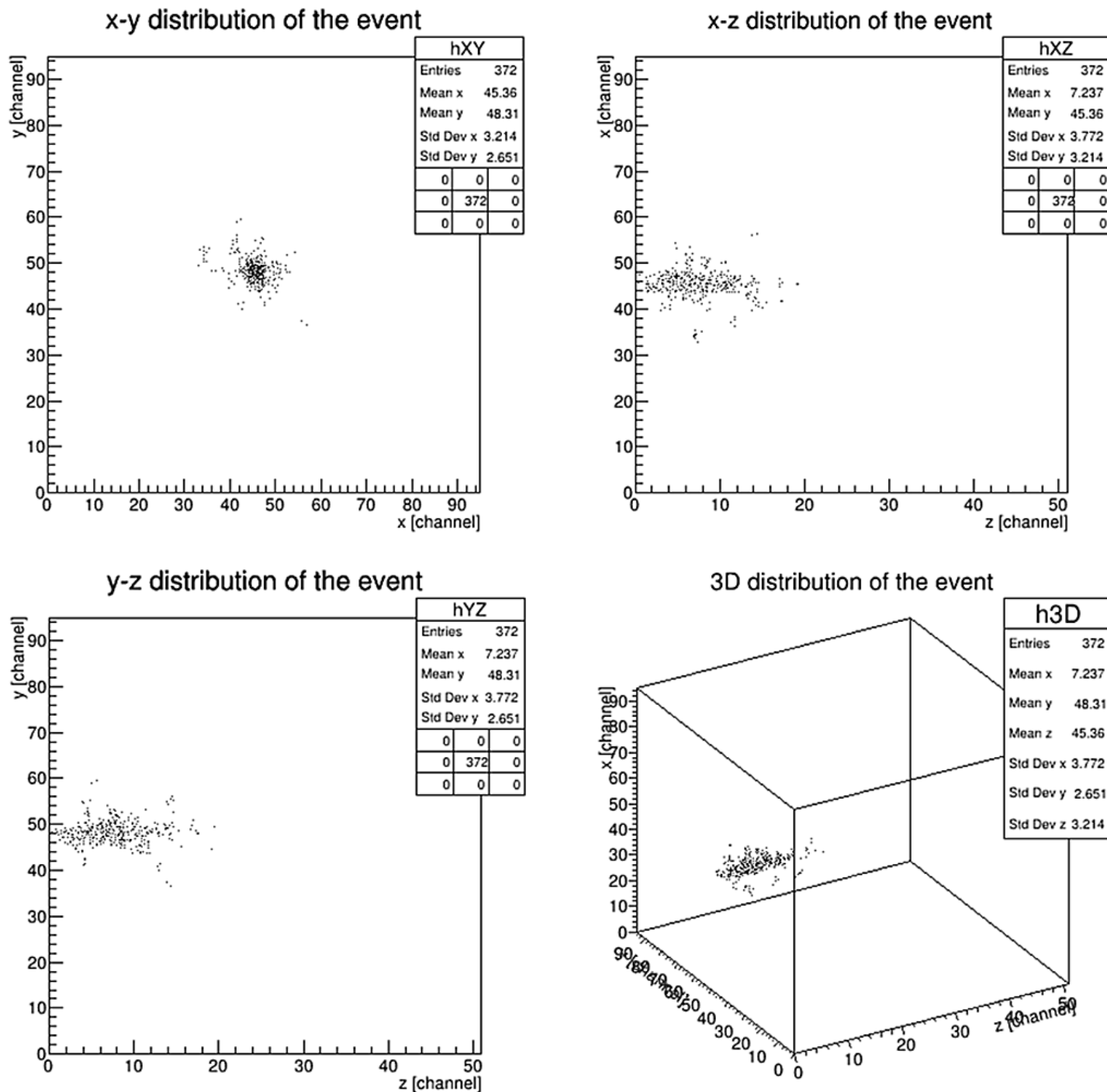


FIGURE 6.8: Projections and 3D view of an electron event from a 60 GeV run.

Energy		16 GeV/c	60 GeV/c	120 GeV/c
Cut	<10 hits	99	99	99
	>4000 hits	99	99	99
	Faulty Z layers	92	85	75
	Multiple entries	100	99	99
	Too soon	100	100	99
	Surviving Events	91	83	75

TABLE 6.3: Percentage of surviving events for every cut applied consecutively for a typical June 2011 run of 16 GeV, 60 GeV and 120 GeV.

Energy		16 GeV/c	60 GeV/c	120 GeV/c
PID*	Muons	9	0.5	0
	Pions	22	31.5	31
	Electrons /Positrons	59	57	56
	Undetermined	10	11	13

TABLE 6.4: Particle identification (PID) percentage of the surviving events. *Undetermined* refers to the surviving events that were not matched to a muon event, a pion event or an electron/positron event. *Particle identification percentage of the surviving events.

6.2.5 Surviving Events

In general, the percentage of surviving events of a run is high at low energies and low at high energies as it can be inferred from Table 6.3 where the results of the selection cuts from three typical runs at low, medium and high energy are listed. As for the particle identification results presented in Table 6.4, it appears that the test beams are mainly composed of electrons while muons are a minority which disappears at high energy. At any energy, pions are present in a proportion that is slightly less than half the electrons. Table 6.5 summarizes the total number of events that was found before and after the selection cuts for all energies.

Energy	Raw number of events	Number of events after selection cuts
8 GeV	139,536	129,755
16 GeV	173,899	153,985
32 GeV	232,715	148,982
40 GeV	204,741	160,820
50 GeV	135,221	98,712
60 GeV	110,223	87,077
120 GeV	157,664	120,860

TABLE 6.5: Raw number of events found within all runs of a specific energy and the corresponding number of surviving events.

Chapter 7

Calibration

The purpose of calibration is to linearize the response of the detector with respect to energy, angle of track segments, time, environmental conditions, etc. Ideally, a detector's response should be the same at all times but in practice, the experimental factors mentioned above change from period to period if not from run to run. As such, a calibration scheme is a good way to measure the importance of a certain factor over another, ascertain its stability and to ensure smooth detector performance after appropriate calibration.

7.1 Efficiency

The efficiency ε_i measures the detector's response to an incoming particle at RPC level. It takes an average value between 1 and 0 for each RPC in the DHCAL. For each track segment, the parametric 3D line is computed. For each RPC_i , traversed by the parametric line, 1 is added if at least 1 hit (i.e. 1 cell fired) was recorded in the RPC for this segment, else it is a gap and 0 is added. After processing all segments, the sum for each RPC_i is divided by the total number of segments which traversed RPC_i .

$$\varepsilon_i = \frac{\sum X_{RPC_i}}{\text{total number of segments traversing } RPC_i} \quad (7.1)$$

$$X_{RPC_i} = \begin{cases} 1, & \text{if } \geq 1 \text{ hits recorded} \\ 0, & \text{if there is a gap} \end{cases}$$

7.2 Multiplicity

The multiplicity μ_i measures the average number of cells firing (or *hits*) for a single segment recorded traversing RPC_i . For each RPC, the number of hits recorded when traversed by a segment which fired at least one cell is added. If no hits were recorded in RPC_i , the segment is not counted in the total number of segments traversing RPC_i . After processing all the segments, the sum for each RPC_i is divided by the total number of segments which traversed RPC_i .

$$\mu_i = \frac{\sum \text{number of cells fired}}{\sum X_{RPC_i}} \quad (7.2)$$

7.3 Calibration factor

The calibration factor c_i corrects the number of hits recorded by a RPC_i at an energy E .

$$c_i = \varepsilon_i \mu_i = \frac{\sum \text{number of hits}}{\sum \text{number of segments}} \quad (7.3)$$

μ_i and ε_i are calculated to better understand detector behavior.

7.4 Overall calibration factor

The calibration factor c_i corrects the number of hits recorded by a RPC_i at an energy E .

$$c_i = \frac{\varepsilon_i \mu_i}{\varepsilon_0 \mu_0} \quad (7.4)$$

Where:

ε_0 : Average efficiency over all the RPCs of one run

μ_0 : Average multiplicity over all the RPCs of one run

This ensures consistent calibration for all runs of a data taking period.

Chapter 8

Track Segment Analysis

8.1 Track Segments Analysis in CALICE Calorimeters

Thanks to the high granularity of its PFA based calorimeters, the CALICE collaboration opens the door to detector calibration using track segment analysis under the MIP assumption. The secondary particle tracks are then treated as MIP tracks. This type of calibration could be used in-situ during an experiment without the necessity of a pause in order to use a dedicated calibration run.

8.1.1 AHCAL

In 2010, the AHCAL used single particle MIP tracks in hadronic showers for calibration. The tracks were found by a searching method that looks for isolated hits and treats them as seeds to search for neighboring isolated hits in the next layer, in the beam direction, until the end of the detector or the lack of close isolated hits. This method makes it possible to track long term variations in the detector and could be used in situ instead of using dedicated runs. The results agreed with the simulated data[28].

8.1.2 SDHCAL

In 2016, the SDHCAL used pion tracks from hadronic test beams taken at CERN SPS in 2012 for calibration and achieved a positive improvement of the energy resolution up

to $\frac{30\%}{\sqrt{E(\text{GeV})}}$ for 80 GeV pions[9]. In 2017, the SDHCAL applied a Hough method search to identify hadronic shower tracks from the same test beams mentioned earlier, and used them for calibration. The results were observed to be generally consistent with the simulated data. In addition, the energy resolution obtained in 2016 were slightly improved by a few percents. An increase of RPC efficiency and multiplicity compared to muon test beams was observed due to the fact that some hadronic tracks were not collinear with the detector's main axis. The small angle in the trajectory increases the matter traversed by the off-beam axis tracks, thus increasing the probability of multiple hits being registered for a single point of entry[12].

8.1.3 DHCAL

Muon MIP tracks or track fits from dedicated muon runs at FermiLab and CERN were used to study the DHCAL response[24] and a first study using hadronic shower tracks or track segments for calibration was conducted in 2013. A nearest neighbor search algorithm identified the tracks which were then fitted to 3D lines. An improvement of the mean response and resolution was observed[7]. In 2015, the use of track segments belonging not only to hadronic showers and muons but also to electromagnetic showers to calibrate the DHCAL was initiated [15]. It is developed and expanded in this thesis.

8.2 Segment Selection

8.2.1 Identifying Clusters

The first step of the track analysis is to find and identify good clusters which will be treated as track segments.

An event corresponds to the entry of a particle and its hadronic or electromagnetic shower when it is not a muon MIP track. In the case of a particle shower, the core of the shower where the density of hits is too high to resolve any secondary particle tracks must be removed, least the number of hits in a cluster be overestimated or the spacial distribution be disrupted. The secondary particle tracks are approximated to first order as MIP tracks.

When the core of a shower has been removed, cluster identification can begin. A boolean map is created which spans the whole 96x96x38 3D coordinates of the DHCAL main stack. 1's are stored at the coordinates where hits occur, 0's otherwise. A connectivity map is created after summing the number of neighbors for each 3D detector coordinates. Neighbors living in adjacent layers are also counted. To first order, one coordinate has 26 neighbors. The order can be changed to include further hits. Dense cores are rejected if the connectivity is higher than 8. Isolated hits are also rejected. This step is repeated to reject smaller cores and isolated hits created by the first iteration of the connectivity map. Clusters are found by joining connecting hits.

Finally, clusters with an equal or higher number of hits than the threshold value, **NHits**, are kept and stored into a list of single hits. These single hits are saved to be later combined with identified segments under special conditions detailed in the following section. The selection of $\text{NHits} = 9$ is discussed later in Section 8.2.3.

8.2.2 Segment Selection

Ideally, segments are straight tracks with as little dispersion as possible such that the hits follow a line oriented along incident beam direction.

However, the discretization of the detector into cells as well as the detector's geometry impose a limit on the quality of the tracks. As will be explained in further details in Section 8.4, particles propagating in the DHCAL with a non-zero polar angle θ are expected to record a factor $\frac{1}{\cos\theta}$ more hits than tracks collinear with the detector's main axis (i.e $\theta = 0^\circ$). This can lead to an overestimation of a segment energy since more hits are recorded in this case than for a horizontal segment of the same energy. Despite the event selection cuts, it is possible that some surviving clusters are unphysical clouds of hits due to electronic noise or faulty cells.

The orientation and barycenter of a cluster are found using the discrete inertia tensor

$$\mathbb{I} = \sum_{i=1}^N \begin{pmatrix} y_i^2 + z_i^2 & -x_i y_i & -x_i z_i \\ -x_i y_i & x_i^2 + z_i^2 & -y_i z_i \\ -x_i y_i & -y_i z_i & x_i^2 + y_i^2 \end{pmatrix} \quad (8.1)$$

which can be rewritten as a diagonal matrix in terms of its three eigenvalues e_1 , e_2 and e_3 after solving for its eigenvectors \vec{v}_1 , \vec{v}_2 and \vec{v}_3 :

$$\mathbb{I} = \sum_{i=1}^N \begin{pmatrix} e_1 & 0 & 0 \\ 0 & e_2 & 0 \\ 0 & 0 & e_3 \end{pmatrix} \quad (8.2)$$

In this context, the eigenvalues are the moments of inertia around the cluster's principal axes corresponding to the eigenvectors. The longest principal axis has the smallest eigenvalue; in this thesis, e_1 will denote this quantity. The transverse eigenvalue $e_T = \sqrt{e_2^2 + e_3^2}$ is the cluster's transverse size. The eigenvalue ratio, $\frac{e_1}{e_T}$, is a measure of the cluster's likeness to a straight line. The smaller this quantity is, the better the cluster can be likened to a straight line. Only clusters with $\frac{e_1}{e_T} < 0.1$ are kept during segment selection.

8.2.3 Tuning of NHits

NHits is the minimum number of hits for a cluster to be considered a segment candidate. The higher the value is, the more likely the cluster will be long (i.e. traverse more z layers) and have a better quality (i.e. a small $\frac{e_1}{e_T}$). However, a higher value for NHits will also decrease the number of surviving clusters, thus limiting the statistics of the subsequent track segment analysis.

Integer NHits values between 6 and 12 inclusive were tested when finding segments for the muon, pion and electron events of a 60 GeV run (Figure 8.1, Figure 8.2 and Figure 8.3 respectively). As predicted, the number of segments decreases as NHits increases for all particle types although this effect is more drastic for pions and electrons. Since muon tracks are generally long tracks (Chapter 6), it is not surprising that the number of muon clusters has a slower decrease. The average $\frac{e_1}{e_T}$ decreases slightly as NHits increases for all particle types, and reaches a plateau around NHits = 10 hits for muons and NHits = 9 hits for pions and electrons. This observation motivates the choice to use NHits = 9 hits such that cluster quality is maximized while preserving a high number of segments.

The average number of layers traversed by the clusters increases with NHits as expected for all particle types even more so for muons.

Energy	Muon segments	Pion segments	Electron segments
8 GeV	38,446	8,845	3,284
16 GeV	22,427	21,243	27,047
32 GeV	9,214	37,340	39,631
40 GeV	4,669	38,281	71,519
50 GeV	1,342	23,474	43,310
60 GeV	600	15,859	29,197
120 GeV	75	12,244	23,130

TABLE 8.1: Total number of segments per particle type identified for all runs of a same energy.

The average ratio of hits divided by the number of traversed layers gives an image of the average multiplicity of hits per layer. This quantity decreases with NHits and plateaus around 2 hits/layers for pions and electrons, while it does so around 1.2 hits/layers for muons. This is to be expected as muon tracks have less dispersion than the other particles tracks. Also, they are less likely to fire neighboring cells around their point of entry because they propagate along the beam axis which is the same as the DHCAL's main axis. This is not the case for electrons and pions generated at an angle with respect to the DHCAL main axis. This angle difference increases their path length in the detector's matter, thus increasing the probability of interaction leading neighboring cells firing.

Figures 8.4 and 8.5 also illustrate the effect of varying NHits on cluster identification at each end of the available energy range for pion events of a 16 GeV run and a 120 GeV run respectively. The trends described for 60 GeV are apply for 16 GeV and 120 GeV with little difference. The average ratio of hits divided by the number of traversed layers plateaus at 1.6 hits/layers at 16 GeV and at 2.4 hits/layers at 120 GeV. It appears that this quantity increases with incoming particle energy. The eigenvalue ratio does not plateau around NHits = 9 hits at 16 GeV but at NHits = 12 hits. This represents a decrease of $\sim 20\%$ in quality when choosing fixing NHits to 9 hits but this alternative preserves $\sim 60\%$ more segments.

Table 8.1 summarizes the results of segment identification for all runs of all energies by presenting the total number of identified segments per particle type.

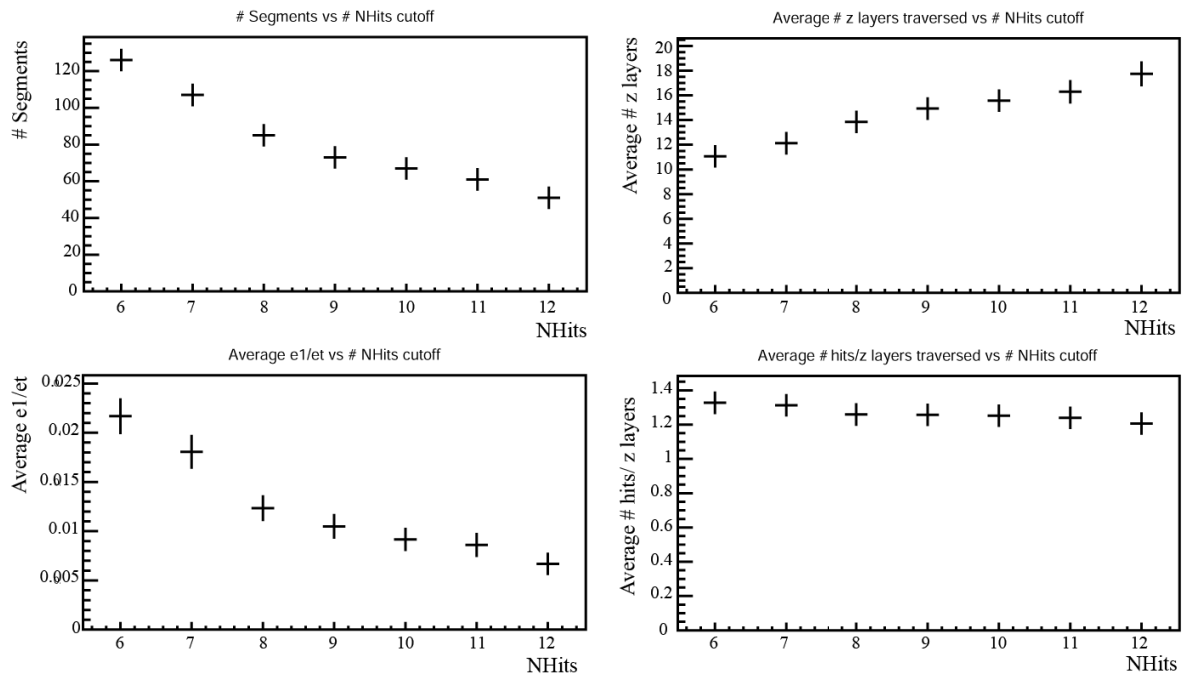


FIGURE 8.1: (From left to right, top to bottom) Effects of varying NHits on the number of segments, the average number of layers traversed, the average eigen_ratio and average number of hits per layer traversed on the **muon** events of a **60 GeV** run.

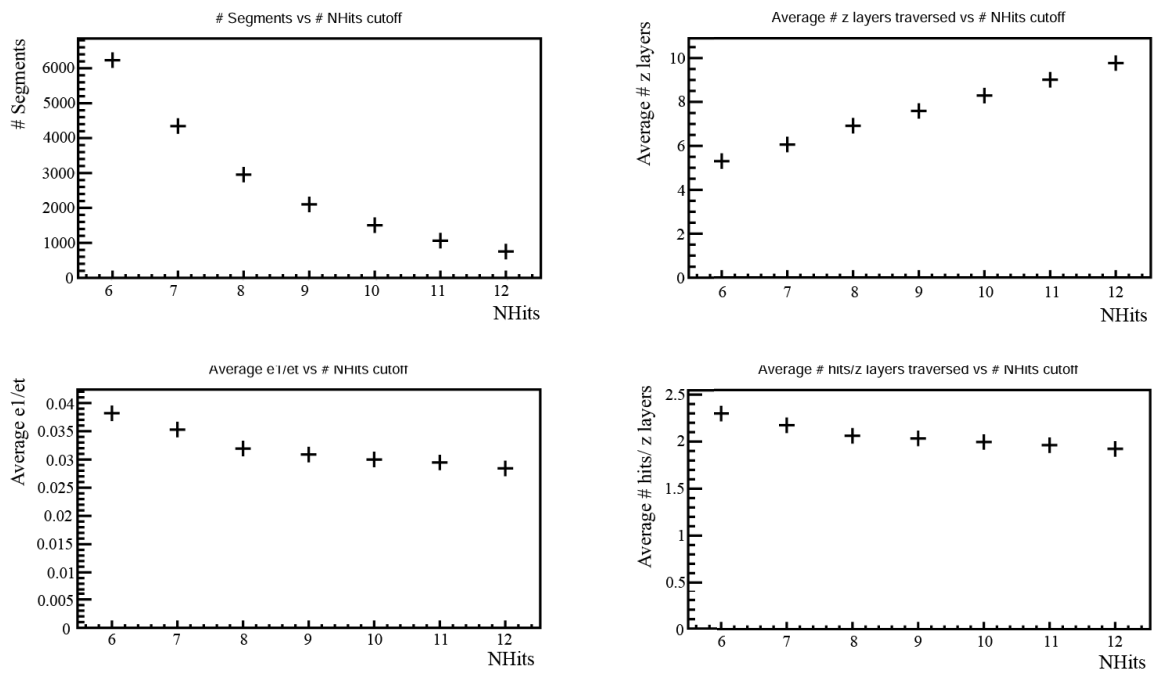


FIGURE 8.2: (From left to right, top to bottom) Effects of varying NHits on the number of segments, the average number of layers traversed, the average eigen_ratio and average number of hits per layer traversed on the **pion** events of a **60 GeV** run.

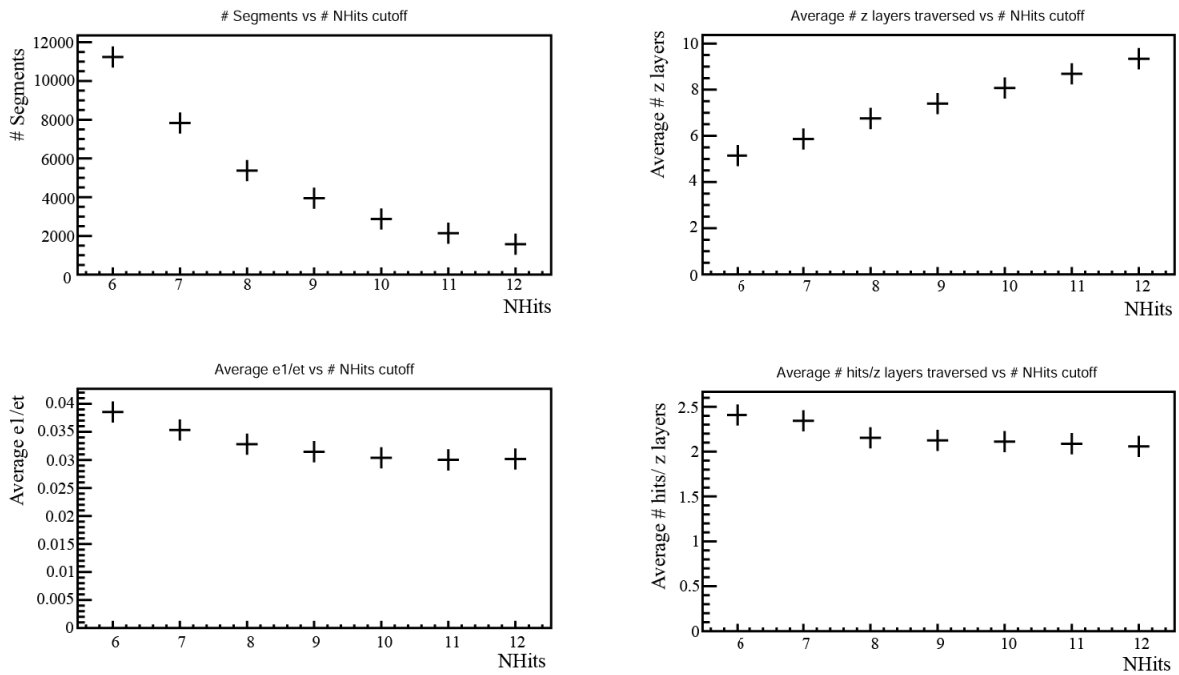


FIGURE 8.3: (From left to right, top to bottom) Effects of varying NHits on the number of segments, the average number of layers traversed, the average eigen_ratio and average number of hits per layer traversed on the **electron** events of a **60 GeV** run.

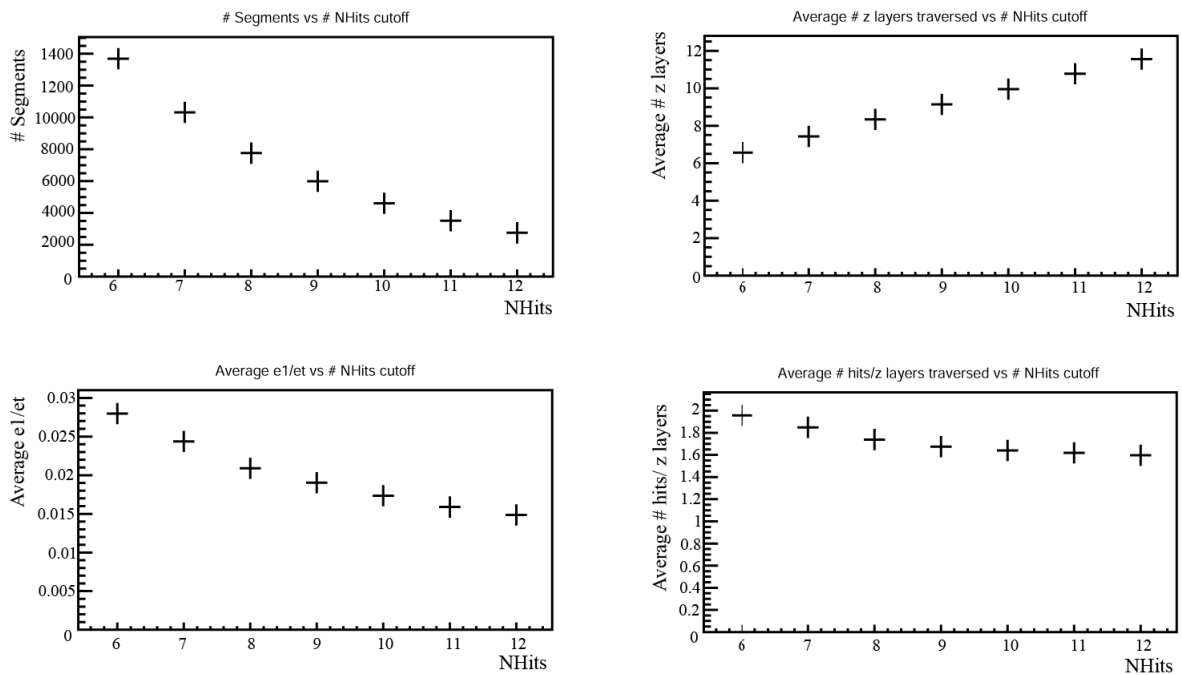


FIGURE 8.4: (From left to right, top to bottom) Effects of varying NHits on the number of segments, the average number of layers traversed, the average eigen_ratio and average number of hits per layer traversed on the **pion** events of a **16 GeV** run.

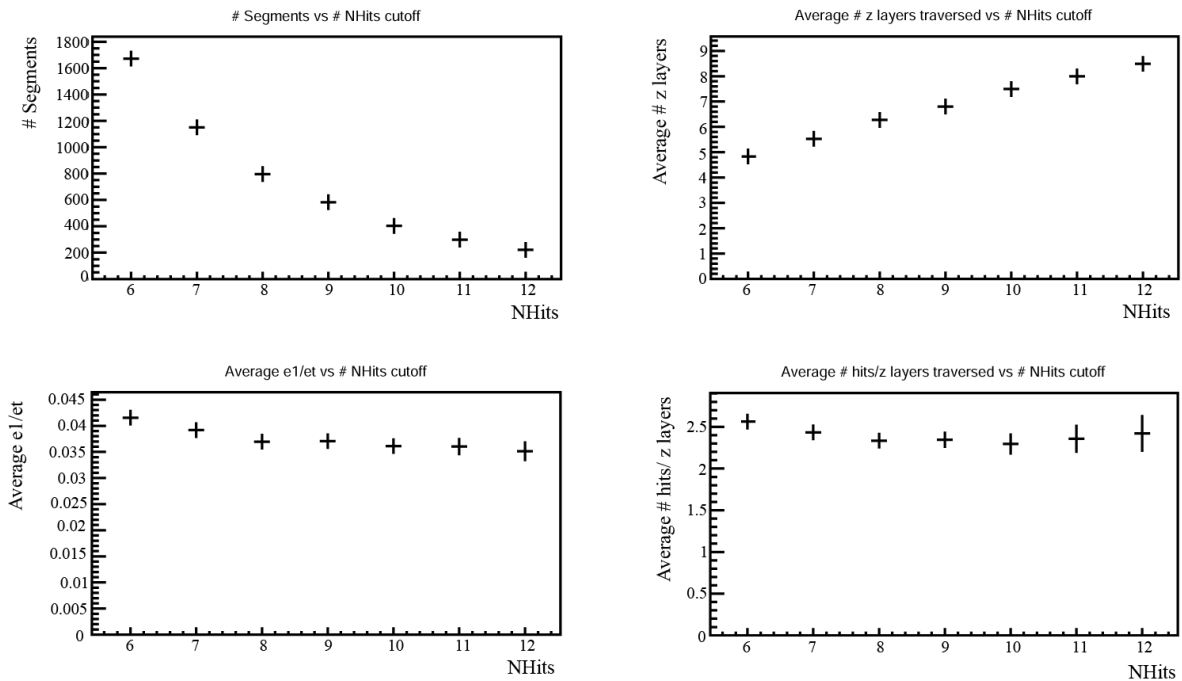


FIGURE 8.5: (From left to right, top to bottom) Effects of varying NHits on the number of segments, the average number of layers traversed, the average eigen_ratio and average number of hits per layer traversed on the **pion** events of a 120 GeV run.

8.3 Combining Segments and Single Hits

To get a complete picture of the DHCAL response, especially detector efficiency, it is important to identify complete tracks with gaps in layers traversed. The merging of already identified segments with one another from the same event, is first considered as some can be portions of longer segments. Secondly, single hits are considered to be added to already identified segments from the same event.

For each set of identified segments from the same event, the segments are ordered in increasing layer coordinate of their first hit, z_0 . The first segment is fitted to a 3D parametric line and so are the other segments. The first segment last hits are extrapolated until the starting layer of the compared segment while the compared segment first hits are extrapolated until the layer of the first segment's last hit.

An intersection plane is estimated such that it is closer to the smallest segment.

The gap between the last hit of the front segment and the first hit of the back segment is divided by the combined length of both segments to get **div**. The intersection is located at the end of the front segment at a distance **div** \times *front segment length*.

If the X and Y coordinates of both segments (X_1, Y_1) and (X_2, Y_2) in the intersection plane are within a radius, **RADI** than the angle between both segments, θ_{max} , is computed. If θ_{max} is less than 5° then both segments can be combined. The selection of **RADI** = 1.5 cells is discussed later in the next subsection. This procedure is repeated until each segment has been considered.

To combine single hits, the newly combined segments and surviving segments from the same event are fitted to a 3D parametric line. Each hit from the event list of single hits, is tested to see if it lives in a circle of radius **RADI** with the center being the fitted hit of the 3D parametric line.

8.3.1 Tuning of RADI

The maximum radius of intersection of two segments considered to be merged in units of detector cells, **RADI**, is the main parameter when combining segments. As mentioned earlier, it is also the same parameter considered when combining single hits to segments. This parameter ensures that two segments are not too far from each other

while the constraint $\theta_{max} \leq 5^\circ$ confirms that the segments can be combined into a single one without worsening the dispersion of the resulting segment. Too large a value for RADI may lead to the merging of segments which are parallel but do not belong to the same line in space. Too small a value will limit the number of merged segments.

RADI values between 0.5 cells and 2 cells included were tested when merging segments for the muon, pion and electron events of a middle energy range run of 60 GeV (Figure 8.6, Figure 8.7 and Figure 8.8 respectively). As expected, the total number of segments decreases as RADI increases for all particle types, implying that segments are merged. The decrease happens in three steps where $RADI \in [0.5, 1[$ cells, $RADI \in [1, 1.5[$ cells and $RADI \in [1.5, 2]$ cells. The first plateau corresponds to the surface covered by a cell centered on (X_1, Y_1) and its four direct neighbors. The second plateau adds the four diagonal neighbors while the third plateau adds a small part of the cells two cells away from the cell centered on (X_1, Y_1) .

These plateaus can also be identified in the increase of the average number of hits per segments with increasing RADI for all particle types. Considering the third plateau, the number of merged segments is not significant for pion and electron events whose percentage of segments combined correspond to 0.2% and 0.3% of all segments of these events respectively. This result is better for muon as 14% of all segments are combined. The variation of RADI did not affect the average ratio of hits per layer traversed suggesting that one was merging similar segments. The addition of single hits did not increase the multiplicity in a significant manner. The same can be noted for the effect of an increased RADI on the $\frac{e_1}{e_t}$.

Figures 8.9 and 8.10 also illustrate the effect of varying RADI when merging segments and single hits for pion events of a 16 GeV run and a 120 GeV run respectively. The trends described for the 60 GeV pion events apply to the pion events at 16 GeV and 120 GeV with the minor exception that a fourth plateau can be identified at $RADI = 2$ cells in decrease of the total number of segments and the increase of the average number of hits per segments with increasing RADI. $RADI = 1.5$ cells was selected to get the highest number of merged segments while not increasing the allowed radius of intersection in such a way that segments two cells apart (i.e ≥ 2 cm apart) could be merged.

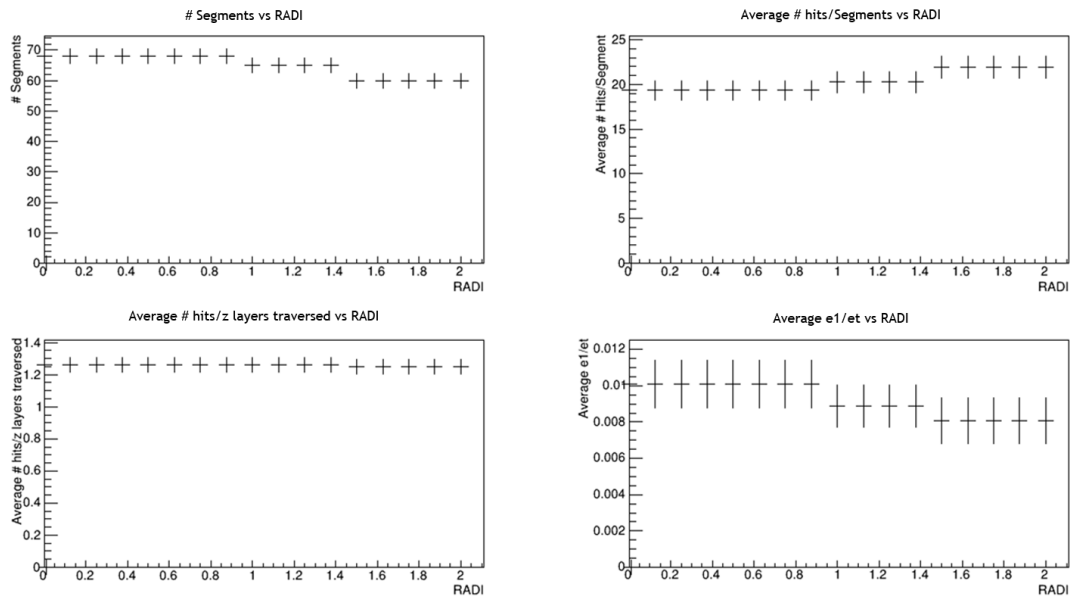


FIGURE 8.6: (From left to right, top to bottom) Effects of varying RADI on the number of segments, the average number of layers traversed, the average eigen_ratio and average number of hits per layer traversed on the **muon** events of a 60 GeV run.

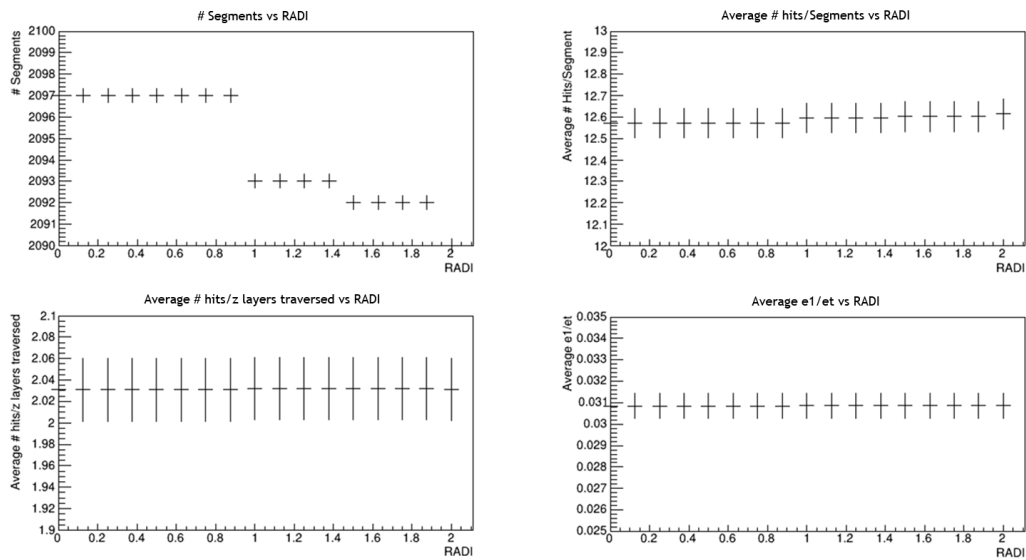


FIGURE 8.7: (From left to right, top to bottom) Effects of varying RADI on the number of segments, the average number of layers traversed, the average eigen_ratio and average number of hits per layer traversed on the **pion** events of a 60 GeV run.

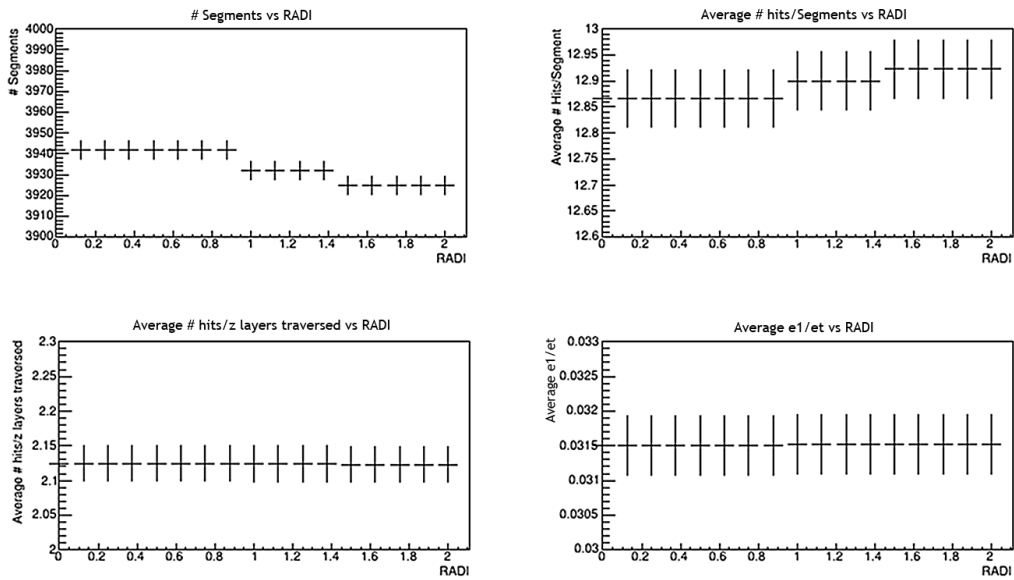


FIGURE 8.8: (From left to right, top to bottom) Effects of varying RADI on the number of segments, the average number of layers traversed, the average eigen_ratio and average number of hits per layer traversed on the **electron** events of a **60 GeV** run.

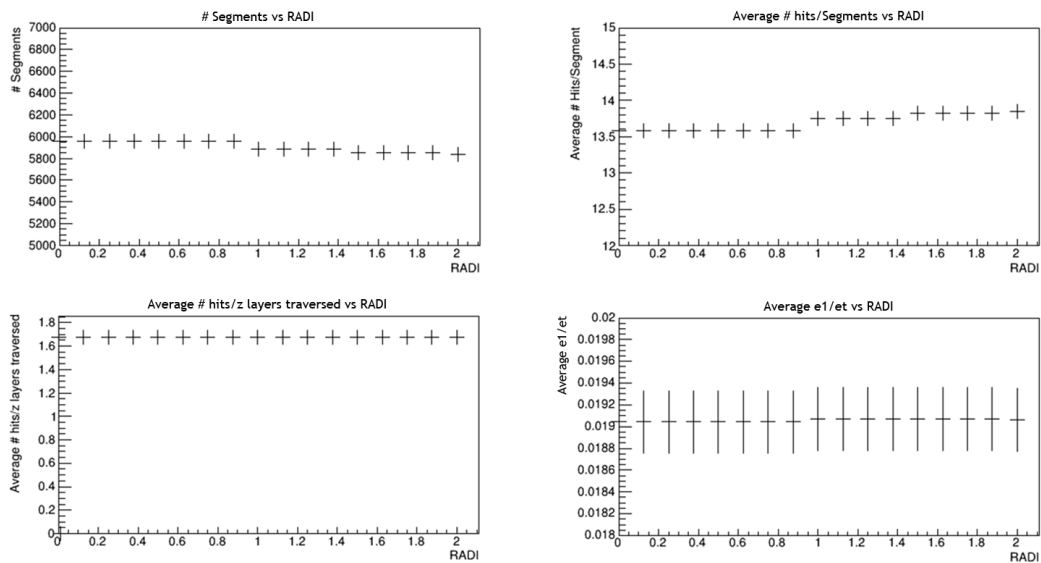


FIGURE 8.9: (From left to right, top to bottom) Effects of varying RADI on the number of segments, the average number of layers traversed, the average eigen_ratio and average number of hits per layer traversed on the **pion** events of a **16 GeV** run.

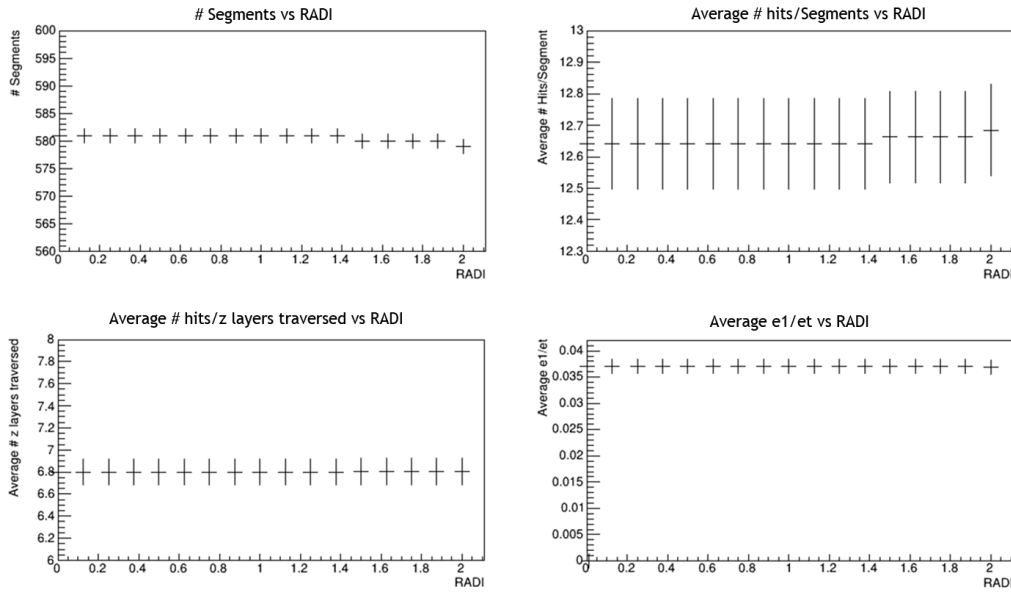


FIGURE 8.10: (From left to right, top to bottom) Effects of varying RADI on the number of segments, the average number of layers traversed, the average eigen_ratio and average number of hits per layer traversed on the pion events of a 120 GeV run.

8.4 Calibration Scheme: Track Segment Angles

8.4.1 Motivation

When a MIP, say a muon, enters the DHCAL along its main axis (Figure 8.11) at a polar angle $\theta = 0^\circ$, its path length L_{0° within detector matter is

$$L_{0^\circ} = nt \quad (8.3)$$

Where:

n : number of traversed layers

t : thickness of a layer

When a MIP track has a non-zero angle of incident θ (Figure 8.12), its total path length in detector matter is increased by a geometrical factor $\frac{1}{\cos \theta}$:

$$L_\theta = \frac{nt}{\cos \theta} = \frac{L_{0^\circ}}{\cos \theta} \quad (8.4)$$

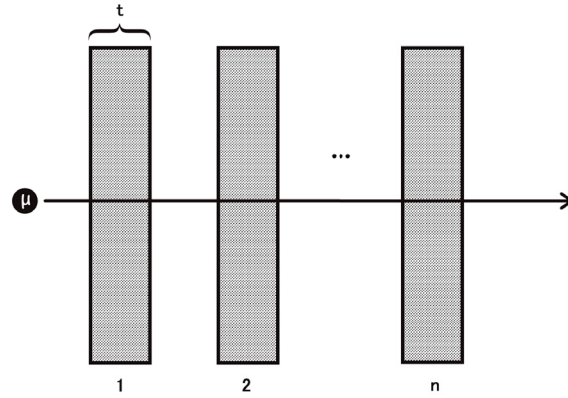


FIGURE 8.11: **Entry of a muon with an incident polar angle $\theta = 0^\circ$ in the DHCAL main stack.** The gray rectangles of thickness t , numbered from 1 to n , represent the DHCAL active layers traversed by the muon. The n^{th} layer is the last one traversed by the muon. The gaps in between layers are actually filled by thick steel absorber plates.

As the path length increases, so does the probability of interaction with the detector leading to many neighboring cells firing instead of one. In other words, the multiplicity at an angle θ , μ_θ , is expected to be increased by the same factor than L_θ :

$$\mu_\theta \propto \frac{\mu_{0^\circ}}{\cos \theta} \approx \mu_{0^\circ} \left(1 + \frac{1}{2}\theta^2 + \frac{5}{24}\theta^4 + \dots \right)$$

Hence, to first order,

$$\mu_\theta = \mu_{0^\circ} + a\theta^2 \quad (8.5)$$

Therefore, it is expected that secondary particle tracks which have a non-zero angle of propagation θ should lead to an increase of recorded hits. To correct for this effect, the calibration factors will be computed such that all segments generate a similar number of hits as if they all had $\theta = 0^\circ$.

8.4.2 Calibration Factors

After parsing all identified segments in a run, a list of all the segments going through a RPC is saved for each RPC of a run. For each RPC, the distribution of the efficiency versus θ is plotted and fitted to a constant to extract ε_{0° relabeled as ε_i , while the multiplicity versus θ is plotted to equation 8.5 in order to get μ_{0° relabeled as μ_i .

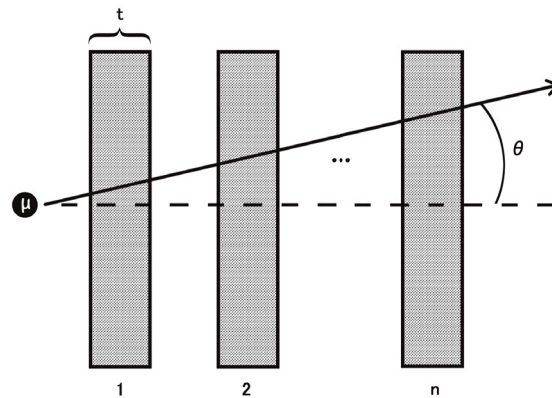


FIGURE 8.12: **Entry of a muon with an incident polar angle θ in the DHCAL main stack.** The gray rectangles of thickness t , numbered from 1 to n , represent the DHCAL active layers traversed by the muon. The n^{th} layer is the last one traversed by the muon. The gaps in between layers are actually filled by thick steel absorber plates.

This procedure yields a much more precise extrapolation at $\theta = 0^\circ$ than it would have been the case by just fitting a subrange like $\theta < 20^\circ$ in the linear portion exclusively, provided that the $\frac{1}{\cos\theta}$ behavior is well represented which is the case here. Furthermore, values at zero angle also establish a more reliable comparison between the different types of particles and other calibration runs with muon beams.

The efficiencies and multiplicities of each segments are computed according to equations 7.1 and 7.2. μ_{0° is taken as μ_i , the multiplicity of one RPC. The response of the RPCs followed the same pattern over all runs and energies. Bottom and top RPCs individually recorded a very small number of segments which resulted in efficiencies and multiplicities with significantly larger errors which were carried into the corresponding calibration factors. In contrast, the middle RPCs, receiving the particle beam head on, recorded a good number of segments.

The same steps are done with all the RPCs together as can be seen in Figure 8.13 and Figure 8.14 in the case of pion, electron and muon events from a 60 GeV run. ε_0 and μ_0 can then be determined from the results. Finally, the calibration factors can be computed in accordance to equation 7.3. One can note that all muon tracks found were practically collinear with the detector's main axis, thus the statistics for $\theta \geq 10^\circ$ is practically nonexistent.

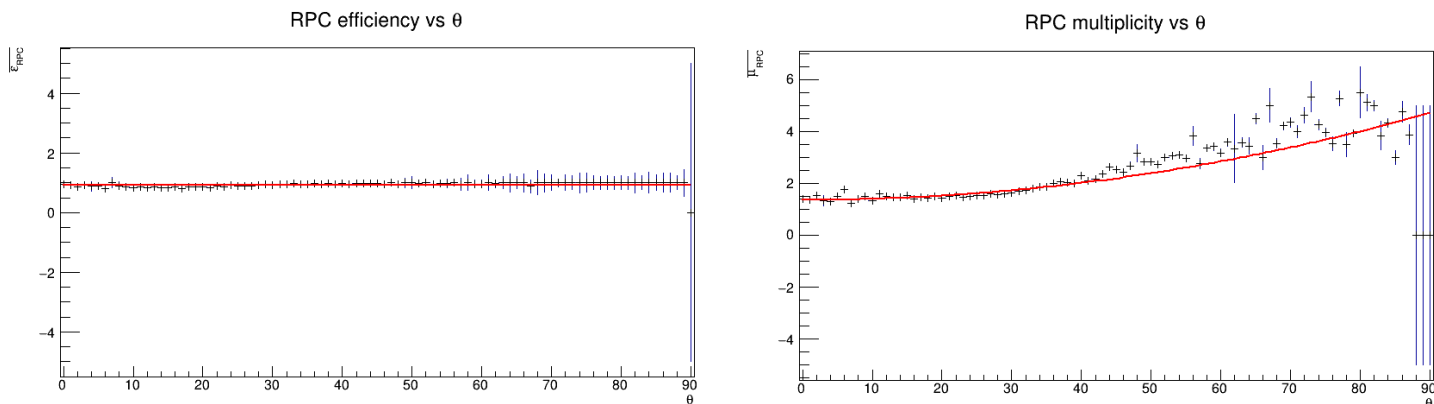


FIGURE 8.13: (Left) **Average RPC efficiency versus θ for pion events at 60 GeV.** The efficiency is essentially one. Note that the uncertainty for $\theta \geq 60^\circ$ is noticeably larger than for smaller angles. There were no segments with $\theta = 90^\circ$ recorded and the error was set to be artificially very big when there is no segment statistics. (Right) Average RPC multiplicity versus θ . The data for $\theta \geq 60^\circ$ is less well described by equation 8.5 (red line) also the uncertainty is higher because less segments were recorded for these angles.

8.4.3 Relative Calibration Results

Figures 8.15 to 8.22 detail the distributions of the average multiplicity, efficiency and calibration factor for all particle types for all runs of the same energy, at energies of 8 GeV, 16 GeV, 32 GeV, 40 GeV, 50 GeV, 60 GeV and 120 GeV after run selection. Note that the horizontal axis lists the run numbers chronologically as they were conducted at Fermilab and that most error bars are obscured by the markers. Run selection was necessary to discard outlier runs from the overall stable response at all energies. Figure 8.18 illustrating the distribution of the calibration factors at 40 GeV before any run selection was operated, offers a good example of the necessity of such a selection. Effectively, run 0 and 2 were discarded from the final results in Figure 8.19 because of their significant deviations from the general trend. The lack of noticeable fluctuations in the final data of all particle types at each energies suggests a stable response of the DHCAL throughout the operation of the test beams.

The distributions of the average multiplicity, efficiency and calibration factor for all particle types and energies are recorded in Figure 8.23. No muon data was available at 120 GeV. The average multiplicity $\bar{\mu}$ and efficiency $\bar{\epsilon}$ are stable for all particle types and

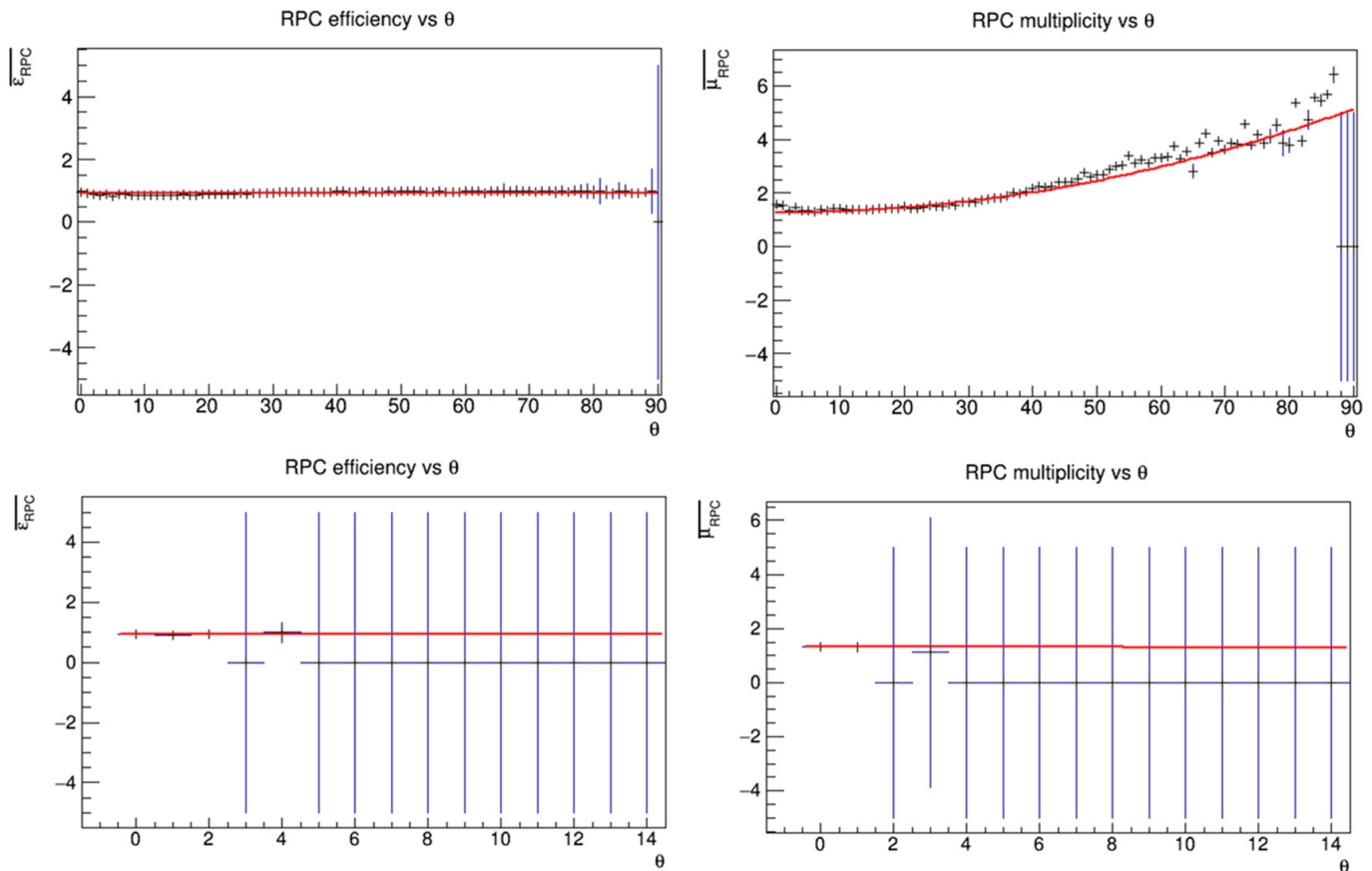


FIGURE 8.14: (Top Left) Average RPC efficiency versus θ and (top right) Average RPC multiplicity versus θ for **electron** events at **60 GeV**. The efficiency is essentially one. There were no segments with $\theta = 90^\circ$ recorded and the error was set to be artificially very big when there is no segment statistics. The multiplicity is less well described by equation 8.5 (red line) for $\theta \geq 45^\circ$. (Bottom left) Average RPC efficiency versus θ and (bottom right) Average RPC multiplicity versus θ for **muon** events at **60 GeV**. Segments with $\theta \geq 4^\circ$ are nonexistent. Both the efficiency and multiplicity are constant at 1 and $1.4 \frac{\text{hits}}{\text{segment}}$ respectively.

energies. All have efficiencies of ~ 0.906 . The trend is modified for the average multiplicities as $\overline{\mu}_\mu \sim 1.315 \frac{\text{hits}}{\text{segment}} > \overline{\mu}_\pi \sim 1.288 \frac{\text{hits}}{\text{segment}} > \overline{\mu}_e \sim 1.252 \frac{\text{hits}}{\text{segment}}$. Evidently, this trend carries to the product of these two variables, namely, the average calibration factor so $\overline{c}_\mu \sim 1.195 > \overline{c}_\pi \sim 1.161 > \overline{c}_e \sim 1.135$. In general, one can note that the calibration factors for all particle types are stable and consistent with each other at all sampled energies with the exception of the muon data at 120 GeV due to the lack of muon events at this energy, confirming the MIP assumption stating that the muons, pions and electrons incident to the DHCAL, as well as the ones generated during particle showers, can all be treated as MIPs (Chapter 8).

Figure 8.24 offers a summary of the results by illustrating the fluctuations in the distributions of average efficiency, multiplicity and calibration for all energies and surviving runs. The efficiency distribution is the most stable one with the least fluctuation between runs of the same energy and specific particle type. As a matter of fact, runs from different particle types and different energies yield similar results. As for the multiplicity distribution, fluctuations are more spread out for runs of the same energy and specific particle type especially for the pion runs at 32 GeV. However, the multiplicity between electron runs and pion runs of different energies remains stable. One should note that the muon data is less consistent with the electron and pion data at energies lower than 40 GeV included. The calibration factor distribution reflects the trends identified in the efficiency and multiplicity distributions. Pions at 32 GeV have the largest spread in calibration factor (0.4) between runs of the same energies and particle types.

Table 8.2 summarizes the results of the relative calibration by listing the average values of the efficiency, multiplicity and calibration factor and their standard deviations per particle type for all energies. The calibration factors between different particle types of the same energy are similar and suggest that the muons, pions and electrons could be treated equally with a common calibration. The stability of the relative calibration is of the order of 1-2% for each energy and 2.8% when considering all energies.

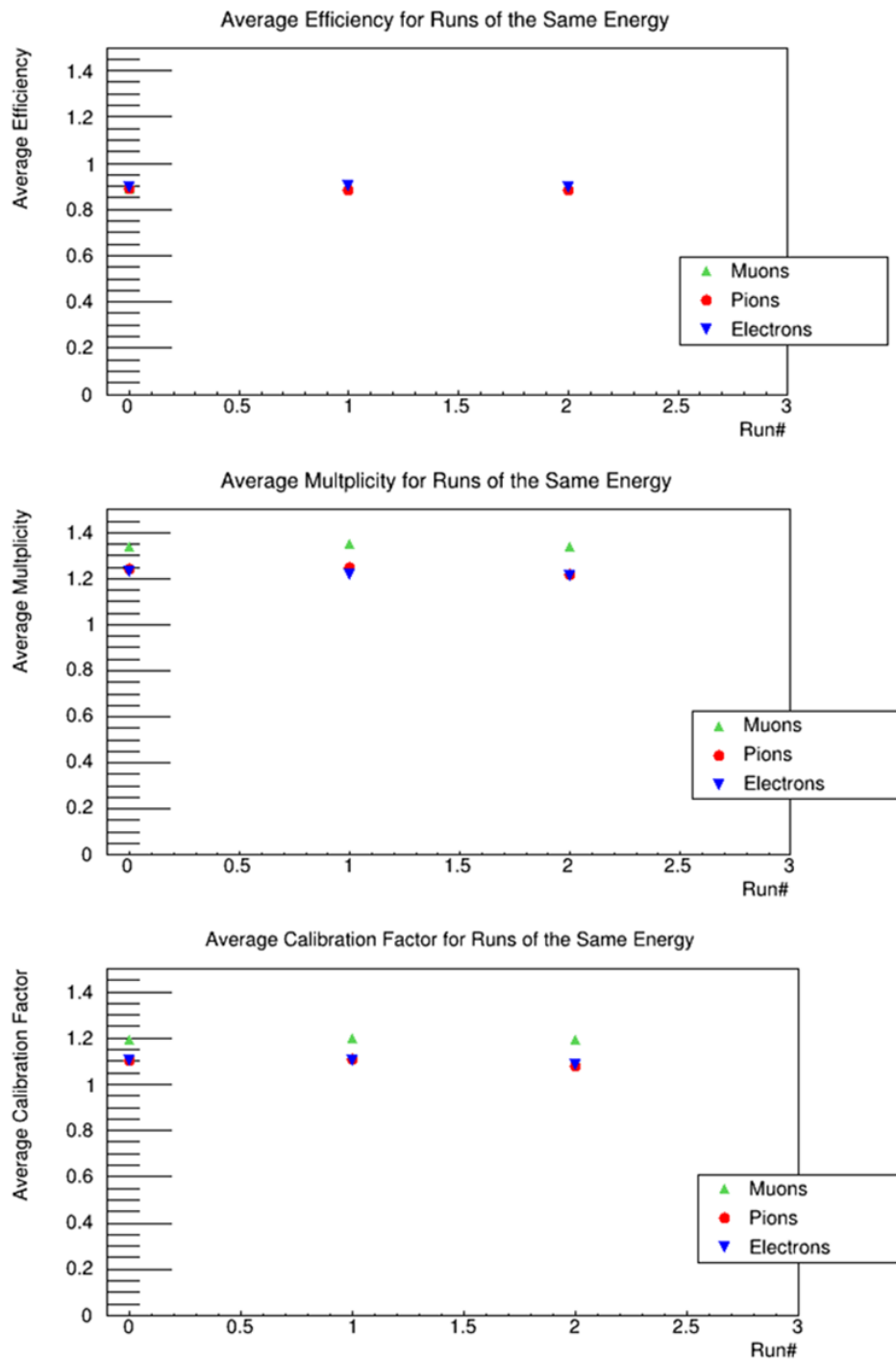


FIGURE 8.15: (Top to bottom) Average efficiency, multiplicity and calibration factor computed for all particle types of all June 2011 runs at 8 GeV. The runs are in chronological order on the horizontal axis. The error bars are obscured by the markers. The efficiencies for all particle types are consistent with each other. The same comment applies to the multiplicities and calibration factors for all particle types of all runs with the exception of the muon multiplicity and calibration factor.

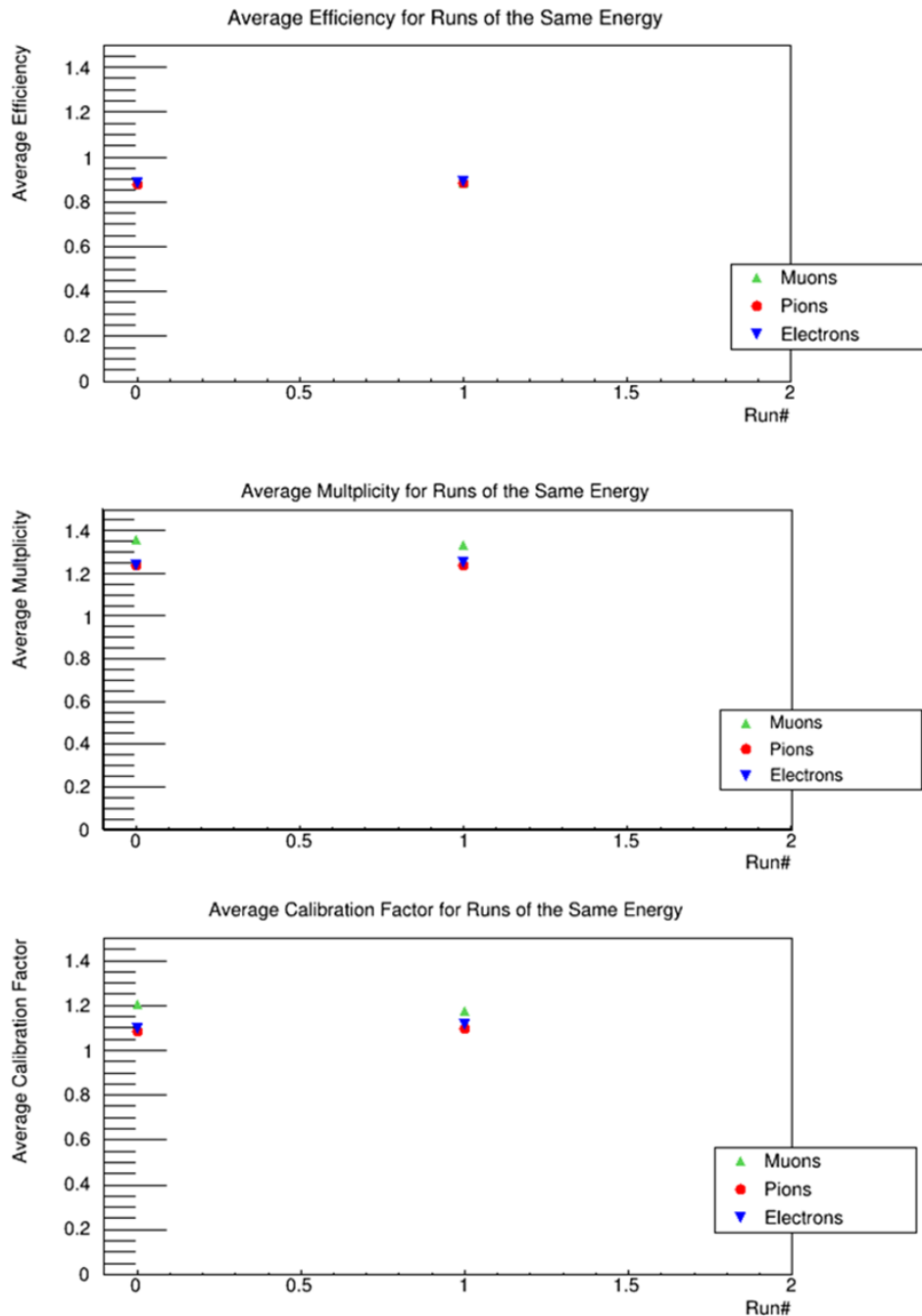


FIGURE 8.16: (Top to bottom) Average efficiency, multiplicity and calibration factor computed for all particle types of all June 2011 runs at **16 GeV**. The runs are in chronological order on the horizontal axis. The error bars are obscured by the markers. The efficiencies for all particle types are consistent with each other. The same comment applies to the multiplicities and calibration factors for all particle types of all runs with the exception of the muon multiplicity and calibration factor.

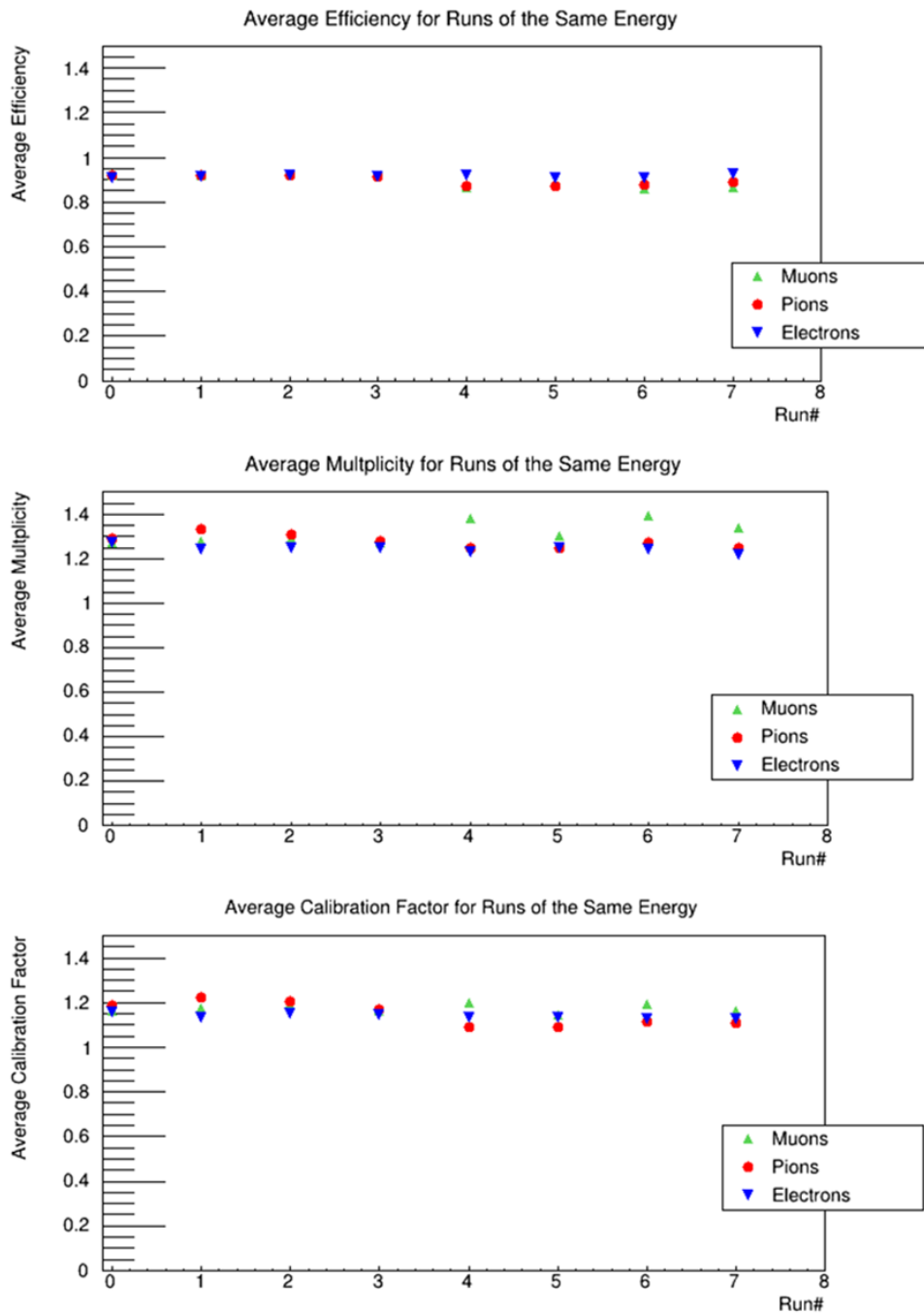


FIGURE 8.17: (Top to bottom) Average efficiency, multiplicity and calibration factor computed for all particle types of all June 2011 runs at **32 GeV**. The runs are in chronological order on the horizontal axis. The error bars are obscured by the markers. The distribution of the average efficiencies and average multiplicities is stable over time for electron and pion tracks but not so much for muon tracks where significant fluctuations are noted for run #4, #6 and #7 in the multiplicity distribution. These comments also describes the distribution of the average calibration factors.

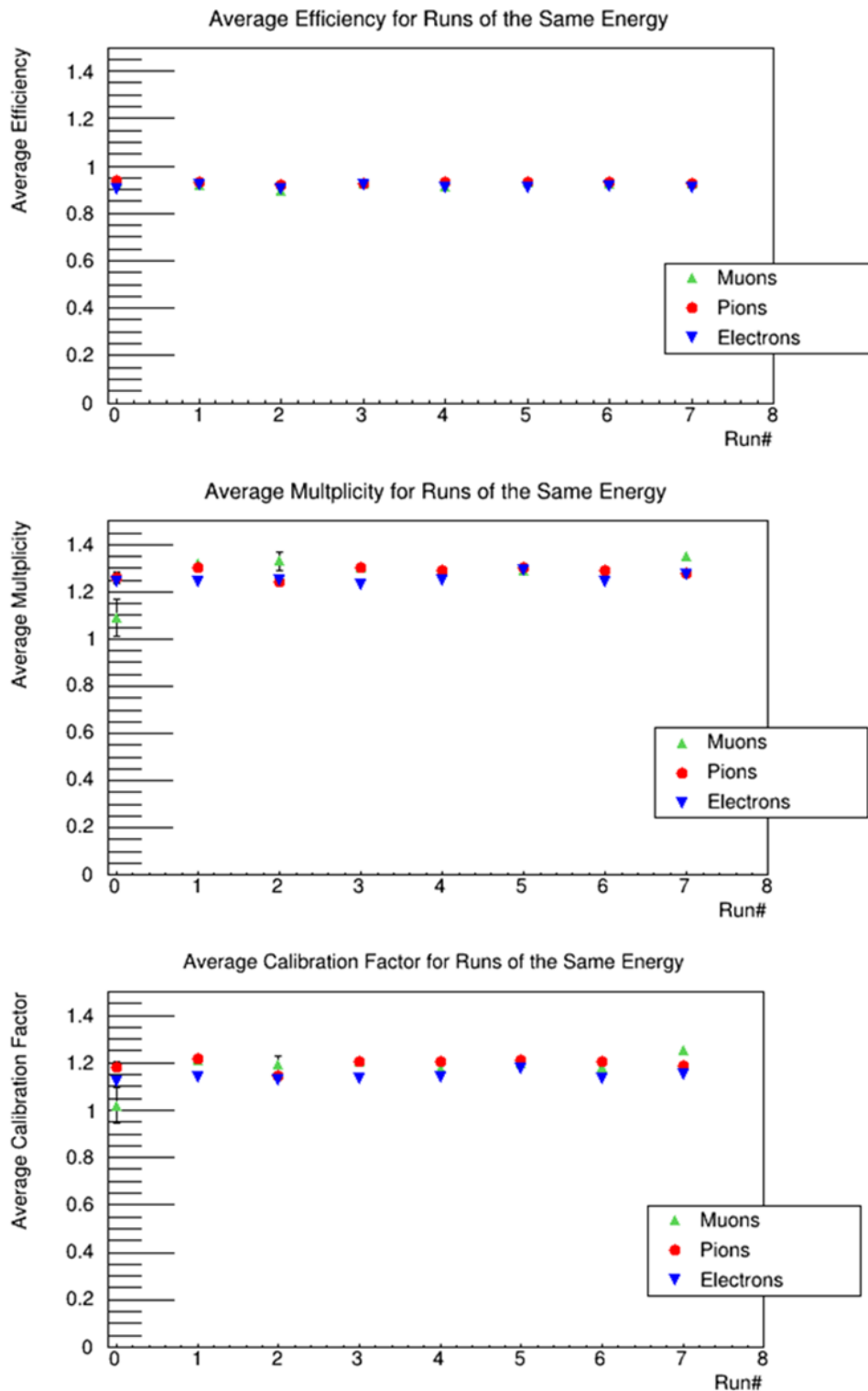


FIGURE 8.18: (Top to bottom) Average efficiency, multiplicity and calibration factor computed for all particle types of all June 2011 runs at 40 GeV before run selection. The runs are in chronological order on the horizontal axis. Most error bars are obscured by the markers. The distribution of the average efficiencies and average multiplicities is stable over time for all particle types except for run 0 and 2.

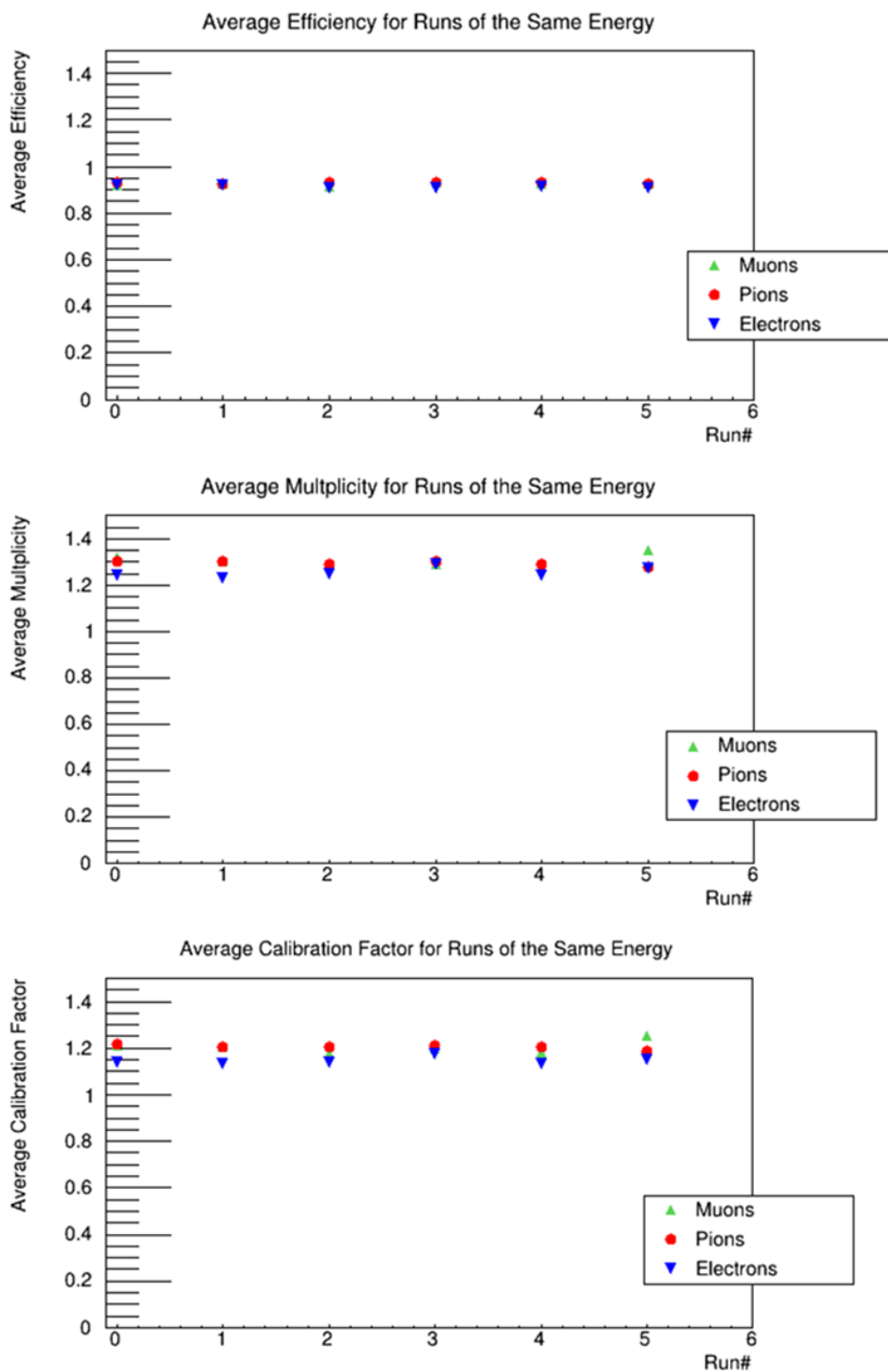


FIGURE 8.19: (Top to bottom) Average efficiency, multiplicity and calibration factor computed for all particle types of all June 2011 runs at **40 GeV**. The runs are in chronological order on the horizontal axis. The error bars are obscured by the markers. The distribution of the average efficiencies and average multiplicities is stable over time for all particle types. These comments also describes the distribution of the average calibration factors.

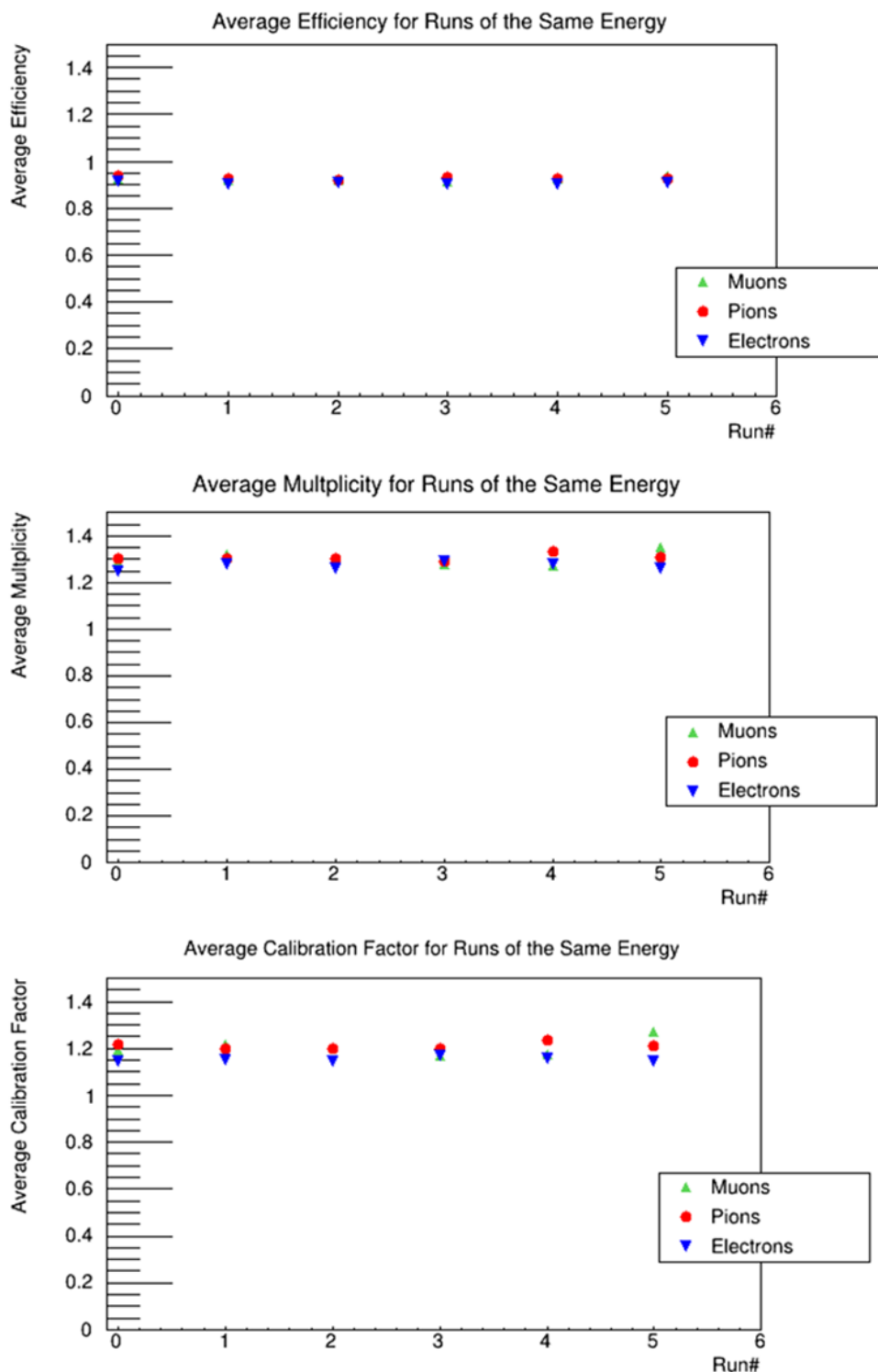


FIGURE 8.20: (Top to bottom) Average efficiency, multiplicity and calibration factor computed for all particle types of all June 2011 runs at 50 GeV. The runs are in chronological order on the horizontal axis. The error bars are obscured by the markers. The distribution of average efficiencies and average multiplicities is stable over time for all particle types. These comments also describes the distribution of the average calibration factors.

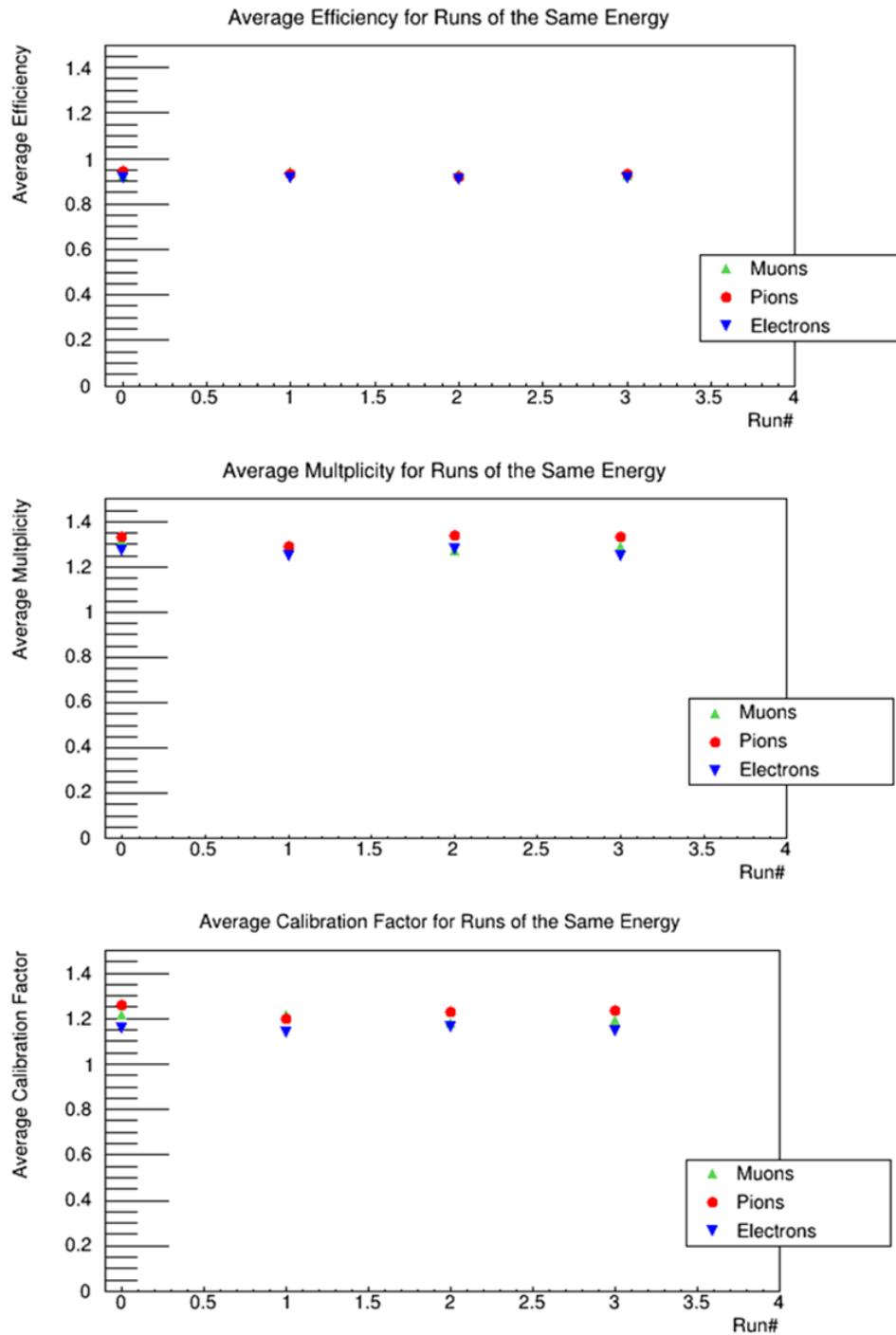


FIGURE 8.21: (Top to bottom) Average efficiency, multiplicity and calibration factor computed for all particle types of all June 2011 runs at 60 GeV. The runs are in chronological order on the horizontal axis. The error bars are obscured by the markers. The distribution of the average efficiencies and average multiplicities is stable over time for all particle types. These comments also describes the distribution of the average calibration factors.

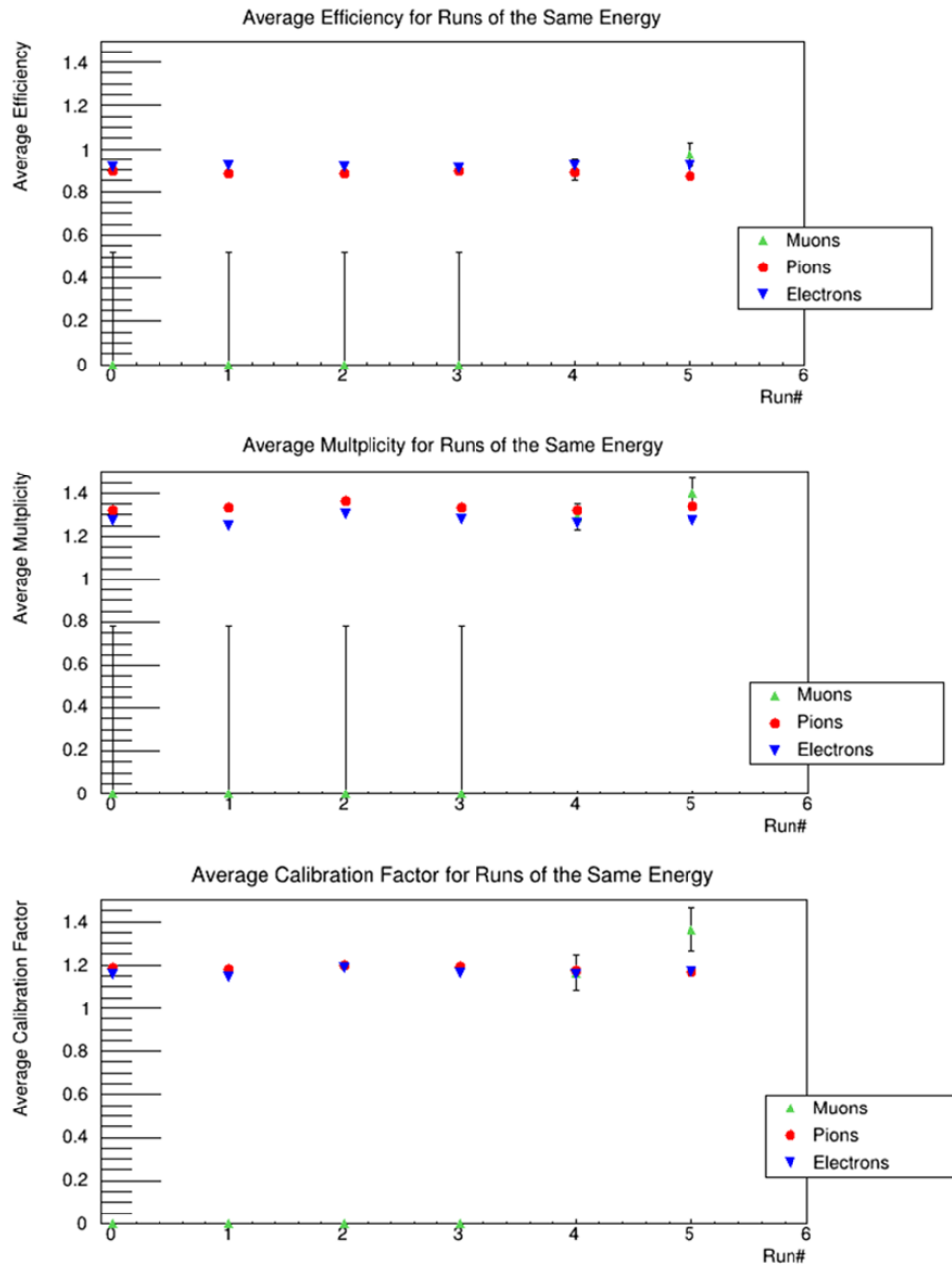


FIGURE 8.22: (Top to bottom) Average efficiency, multiplicity and calibration factor computed for all particle types of all June 2011 runs at **120 GeV**. The runs are in chronological order on the horizontal axis. The error bars for most pion and electron data are obscured by the markers. Muon data is virtually inexistent because of the lack of muon events at 120 GeV (Chapter 6). The distribution of the average efficiencies and average multiplicities is stable over time for all particle types. These comments also describes the distribution of the average calibration factors.

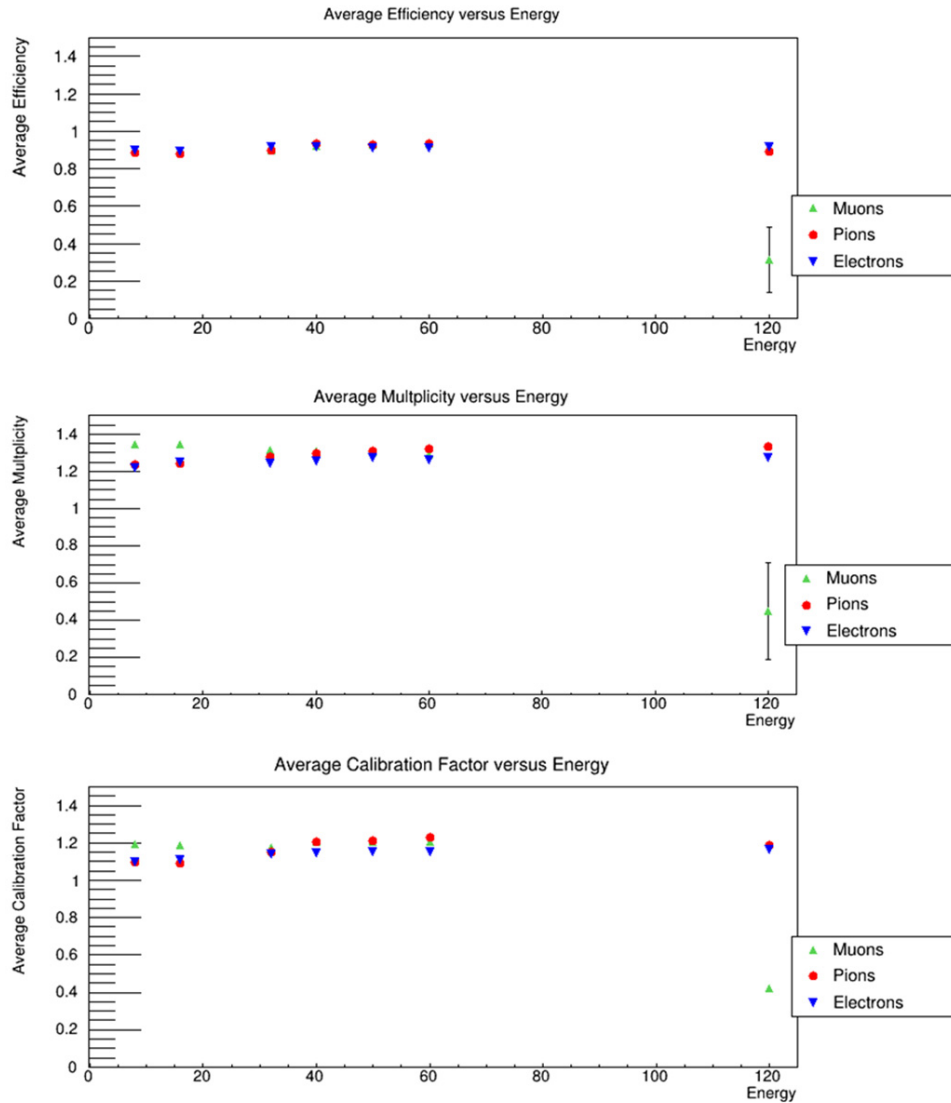


FIGURE 8.23: (Top to bottom) Average efficiency, multiplicity and calibration factor computed for all particle types versus beam energy. The error bars are obscured by the markers. The efficiency, multiplicity and calibration factor are stable for energies higher than 32 GeV for all particle types with the exception of muon tracks at 32 GeV. Detector response at lower energies in the track angle calibration scheme is more erratic.

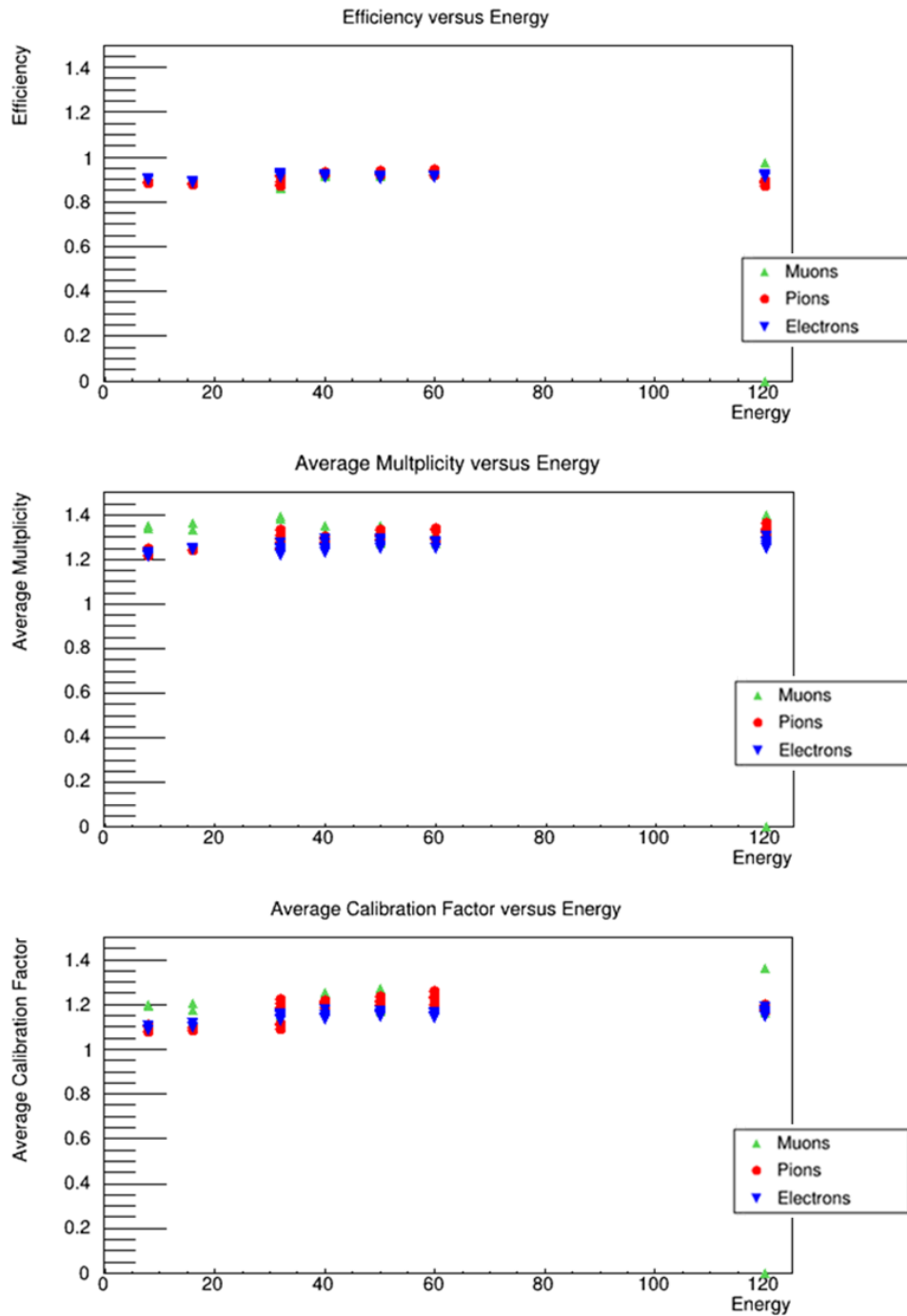


FIGURE 8.24: Distributions of the average efficiency, average multiplicity and average calibration factor for all selected runs at all energies. For each energy, data taking took on average 3 days. The whole of June 2011 data collection spanned 21 days.

Energy	Particle type	Average value			Standard deviation		
		ϵ	μ	c	ϵ	μ	c
8 GeV	muon	0.889	1.343	1.195	0.001	0.005	0.004
	pion	0.886	1.237	1.095	0.001	0.012	0.011
	electron	0.898	1.220	1.096	0.004	0.008	0.010
16 GeV	muon	0.884	1.345	1.188	0.002	0.015	0.015
	pion	0.880	1.245	1.091	0.004	0.005	0.004
	electron	0.888	1.245	1.106	0.004	0.005	0.009
32 GeV	muon	0.894	1.315	1.174	0.026	0.046	0.018
	pion	0.898	1.279	1.149	0.021	0.028	0.135
	electron	0.914	1.244	1.137	0.005	0.014	0.010
40 GeV	muon	0.923	1.305	1.204	0.006	0.024	0.024
	pion	0.931	1.293	1.205	0.003	0.007	0.009
	electron	0.913	1.253	1.144	0.005	0.021	0.014
50 GeV	muon	0.924	1.303	1.204	0.008	0.027	0.033
	pion	0.927	1.305	1.210	0.005	0.013	0.012
	electron	0.907	1.270	1.152	0.005	0.014	0.008
60 GeV	muon	0.930	1.293	1.202	0.007	0.015	0.013
	pion	0.924	1.323	1.230	0.012	0.016	0.017
	electron	0.911	1.263	1.150	0.003	0.011	0.007
120 GeV	muon						
	pion	0.888	1.333	1.184	0.008	0.012	0.010
	electron	0.914	1.272	1.162	0.004	0.015	0.012
All	muon	0.907	1.317	1.195	0.009	0.022	0.018
	pion	0.905	1.288	1.166	0.009	0.013	0.028
	electron	0.906	1.252	1.135	0.004	0.013	0.010
All	all	0.906	1.285	1.164	0.015	0.012	0.028

TABLE 8.2: Average efficiency, multiplicity and calibration factor and their corresponding standard deviations for all energies and particle types. The average efficiencies, multiplicities and calibration factors per particle type are similar across all energies. Averaging these factors per particle type over all energies yields similar efficiencies, multiplicities and calibration factors for muons, pions and electrons. Note that no muon data at 120 GeV was available.

Chapter 9

Discussion and Conclusion

The test beam data performed in June 2011 at Fermilab with the DHCAL at energies ranging from 8 GeV to 120 GeV was analyzed using a new calibration scheme relying on the calorimeter's high granularity. Previous work was done on calibration of the DHCAL with Fermilab November 2011 data at lower energies with the minimal configuration DHCAL using dedicated muon runs[16]. In-situ calibration using particle tracks from analyzed events is ultimately what the ILC is targeting. Preliminary works on a method to analyze track segments from muons, pions and electrons events were conducted at McGill University[15]. This method was further developed to identify track segments from high quality events, infer their particle type from event topology and select high quality segments in order to extract calibration factors.

To test the potential of in-situ track segment calibration, a scheme was selected to investigate the effect of a non-zero polar angle for incoming particles. Geometrical considerations predicted the increase in the number of hits for such tracks compared to incoming particle tracks normal to the detector's surface. The calibration scheme selected corrects the number of hits recorded for off-axis tracks such that they can be compared to on-axis tracks with $\theta = 0^\circ$. By defining two variables to monitor the detector response, the efficiency and the multiplicity, it was possible to compute calibration factors at each energies for surviving runs. The average distributions of these factors for each particle type and energies demonstrated that the impact of a non-zero polar angle is significant for electron and pion tracks but less so for muon tracks. Effectively, the muon tracks found were all collinear with the DHCAL main axis resulting in a lack of statistics for $\theta \geq 10^\circ$. Hence, muon tracks did not need a significant correction to be compared to on-axis tracks.

The distributions of the average multiplicity and efficiency pertaining to the relative calibration which corrects the effect of the non-zero polar angle, revealed that detector response was sensibly independent of beam energy and incident particle type, validating the MIP assumption where muon, pion and electron tracks are all treated as MIP tracks. Indeed, pions and electrons share a stable response throughout time, consistent average efficiencies and multiplicities across all sampled energies (Table 8.2). Muon data is also consistent with pion and electron data with a minimum of fluctuations between different energies with the exception of 120 GeV runs where no muons were available. Further validation by comparing these muon results to dedicated muon beams data using the same calibration scheme could confirm this observation.

One issue which prevented the application of an overall calibration of the DHCAL following the track segment polar angle scheme was the suspiciously high average efficiency recorded at all energies. This result is rooted in the identification of holes within identified tracks stage. For example, it is impossible to know with certainty if the first and last hit in a track are not preceded or followed by a gap which should be included in the track. In consequence, several gaps in particle tracks may have escaped detection thus leading to an inaccurately described RPC response.

Further investigations on the issue raised by the high average efficiency should be conducted before using the track segment angle scheme for an overall calibration of the DHCAL. The development of simulation models of the track segments should be encouraged to further test and validate the calibration.

This scheme results suggested the possibility to apply a common calibration for all particle types and served to showcase the possibility of track segment calibration realized in-situ and its power to monitor detector response without the need for dedicated runs. An absolute calibration may not be possible for track segments alone but the results have demonstrated that a relative calibration could be achieved to monitor calorimeter response and correct calibration in-situ at an order of 2.8% level. Such calibration will prove to be essential in the ILC to save time and cost during the operation of the ILD detector when investigating high energy phenomena.

Bibliography

- [1] Halina Abramowicz et al. “The International Linear Collider Technical Design Report - Volume 4: Detectors”. In: (2013). Ed. by Ties Behnke et al. arXiv: [1306.6329](#) [[physics.ins-det](#)].
- [2] C. Adams et al. “Design, construction and commissioning of the Digital Hadron Calorimeter DHCAL”. In: *Journal of Instrumentation* 11 (2016), P07007. arXiv: [1603.01653](#) [[physics.ins-det](#)].
- [3] Chris Adolphsen et al. “The International Linear Collider Technical Design Report - Volume 3.I: Accelerator & in the Technical Design Phase”. In: (2013). arXiv: [1306.6353](#) [[physics.acc-ph](#)].
- [4] Howard Baer et al. “The International Linear Collider Technical Design Report - Volume 2: Physics”. In: (2013). arXiv: [1306.6352](#) [[hep-ph](#)].
- [5] A. M. Baldini et al. “Search for the lepton flavour violating decay $\mu^+ \rightarrow e^+ \gamma$ with the full dataset of the MEG experiment”. In: *Eur. Phys. J. C* 76.8 (2016), p. 434. DOI: [10.1140/epjc/s10052-016-4271-x](#). arXiv: [1605.05081](#) [[hep-ex](#)].
- [6] Sylvia Berryman. *Ancient Atomism*. Standford, CA, 2005.
- [7] B. Bilki. “CALICE Digital Hadron Calorimeter: Calibration and Response to Hadrons”. In: *LCWS13* (2013). URL: <https://arxiv.org/ftp/arxiv/papers/1404/1404.0041.pdf>.
- [8] B. Bilki and CALICE Collaboration. “The CALICE digital hadron calorimeter: calibration and response to pions and positrons”. In: *Journal of Physics Conference Series*. Vol. 587. Journal of Physics Conference Series. 2015, p. 012038. arXiv: [1404.0041](#) [[physics.ins-det](#)].
- [9] V. Buridon et al. “First results of the CALICE SDHCAL technological prototype”. In: *JINST* 11.04 (2016), P04001. arXiv: [1602.02276](#) [[physics.ins-det](#)].

- [10] M. Chadeeva and for the CALICE collaboration. "Hadron Energy Resolution of the CALICE AHCAL and Software Compensation Approaches". In: *ArXiv e-prints* (2012). arXiv: [1202.6184](https://arxiv.org/abs/1202.6184) [[physics.ins-det](#)].
- [11] CALICE collaboration. "First Results of the CALICE SDHCAL Technological Prototype". In: 11 (Feb. 2016), P04001.
- [12] Z. Deng et al. "Tracking within Hadronic Showers in the CALICE SDHCAL prototype using a Hough Transform Technique". In: *JINST* 12.05 (2017), P05009.
- [13] R. Fabbri. "CALICE Second Generation AHCAL Developments". In: *ArXiv e-prints* (2010). arXiv: [1007.2358](https://arxiv.org/abs/1007.2358) [[physics.ins-det](#)].
- [14] C. W. Fabjan and F. Gianotti. "Calorimetry for particle physics". In: *Rev. Mod. Phys.* 75 (2003), pp. 1243–1286.
- [15] K. Fahrion. "DHCAL Calibration Using Shower Track Segments". In: (2015).
- [16] B. Freund. "The Digital Hadron Calorimeter: Analysis of the November 2011 Fermilab Data". MA thesis. McGill University, 2015.
- [17] David J Griffiths. *Introduction to Elementary Particles; 2nd rev. version*. Physics textbook. New York, NY: Wiley, 2008.
- [18] Particle Data Group. *Passage of particles through matter*. 2014. URL: <http://pdg.lbl.gov/2014/reviews/rpp2014-revpassage-particles-matter.pdf>.
- [19] C. Grupen and B. Shwartz. *Particle Detectors*. Cambridge Monographs on Particle Physics, Nuclear Physics and Cosmology. Cambridge University Press, 2008. ISBN: 9781139469531.
- [20] H. Kapitza K. Edwards. *ZEUS: A Detector for HERA, Letter of Intent*. 1985.
- [21] Tom Kibble. "The Standard Model of Particle Physics". In: 23 (Dec. 2014).
- [22] L. D. Landau. "The Cascade Theory of Electronic Showers". In: *Proceedings of the Royal Society* 166 (1938).
- [23] MissMJ. *Standard Model of Elementary Particles*. 2017. URL: https://commons.wikimedia.org/wiki/File:Standard_Model_of_Elementary_Particles.svg.
- [24] J. Respond. "Calibration of the DHCAL with Muons". In: *Proceedings of Science* (2011). URL: <https://arxiv.org/ftp/arxiv/papers/1202/1202.6653.pdf>.
- [25] M. Thibault. "Test Beam Data Analysis for a Novel Digital Hadronic Calorimeter". In: (2013).

- [26] M. A. Thomson. "Particle flow calorimetry and the PandoraPFA algorithm". In: *Nuclear Instruments and Methods in Physics Research A* 611 (2009), pp. 25–40. arXiv: 0907.3577. URL: <http://adsabs.harvard.edu/abs/2009NIMPA.611...25T>.
- [27] H. Videau et al. "Energy Flow or Particle Flow - The Technique of "Energy Flow" for Pedestrian". In: *International Linear Collider Workshop (LCWS04) Paris, France, April, 2004*. 2004. URL: <https://hal-polytechnique.archives-ouvertes.fr/in2p3-00069714/document>.
- [28] L. Weuste. "Track Segments within Hadronic Showers using the CALICE AH-Cal". In: *International Linear Collider Workshop (LCWS10 and ILC10) Beijing, China, March 26-30, 2010*. 2010. arXiv: 1006.3734. URL: <https://inspirehep.net/record/858847/files/arXiv:1006.3734.pdf>.
- [29] Satoru Yamashita. *ILC Status and outlook*. 2016. URL: https://agenda.linearcollider.org/event/7014/contributions/34798/attachments/30154/45205/ILC_Status_Board_20160602-ECFALC-V3.pdf.

List of Abbreviations

AHCAL	A analog H adron C alorimeter
APD	A valanche P hotodiode
ASIC	A pplication- S pecific I ntegrated C ircuit
ATLAS	A T oroidal L HC A pparatu S
CERN	C entre d'Étude et de R echerche N ucléaire
CLIC	C ompact L inear C ollider
CMS	C ompact M uon S olenoid
DAQ	D ata A cquisition
DHCAL	D igital H adron C alorimeter
ECAL	E lectromagnetic C alorimeter
GRPC	G lass R esistive P late C hamber
HARDROC	H adronic R PC D igital C alorimeter R ead- O ut C hip
HCAL	H adron C alorimeter
ILD	I nternational L inear D etector
LEP	L arge E lectron- P ositron C ollider
LHC	L arge H adron C ollider
LLC	L inear C ollider C ollaboration
MIP	M inimum I onizing P articles
PFA	P article F low A lgorithm
PID	P article I Dentification
QCD	Q uantum C hromatodynamics
QED	Q uantum E lectrodynamics
QFT	Q uantum F ield T heory
RMS	R oot M ean S quare
RPC	R esistive P late C hamber
SDHCAL	S emi D igital H adron C alorimeter
SiD	S ilicon D etector
SiPM	S ilicon P hotomultiplier

TCMT Tail Catcher and Muon Tracker